J. Mech. Phys. Solids 173 (2023) 105222

Contents lists available at ScienceDirect

Journal of the Mechanics and Physics of Solids

journal homepage: www.elsevier.com/locate/jmps

Crack-parallel stress effect on fracture energy of plastic hardening polycrystalline metal identified from gap test scaling

A. Abdullah Dönmez [a,b], Hoang T. Nguyen [c], Houlin Xu [b], Zdeněk P. Bažant [d,*]

[a] Istanbul Technical University, Turkey
[b] Northwestern University, United States of America
[c] Brown University, United States of America
[d] McCormick Institute Professor and W.P. Murphy Professor of Civil and Mechanical Engineering and Materials Science, Northwestern University, 2145 Sheridan Road, CEE/A135, Evanston, IL 60208, United States of America

ARTICLE INFO

Keywords:
Ductile fracture
Aluminum
Fracture experiments
Structural strength scaling
Size effect
Scaling laws
Fracture energy dissipation
J-integral
Material toughness
Asymptotic matching

ABSTRACT

The gap test is a new type of fracture test developed in 2020, in which the end supports of a notched beam are installed with gaps that close only after the elasto-plastic pads next to notch introduce a desired constant crack-parallel compression σ_{xx} (also called the T-stress). The test uses the size effect method to identify how such a compression alters the material fracture energy, G_f, and the characteristic size c_f of the fracture process zone (FPZ). In 2020, experiments showed that a moderate σ_{xx} doubled the G_f of a quasibrittle material (concrete) and a high σ_{xx} reduced its G_f to almost zero. A preliminary study by Nguyen et al. (2021) showed that the gap test can be extended to plastic-hardening polycrystalline metals. A generalized scaling law with an intermediate asymptote for large-scale yielding in small structures was derived, and limited tests of aluminum alloy showed its applicability. In this study, geometrically scaled gap tests of notched three-point bend fracture specimens of aluminum are conducted at three different levels of σ_{xx}. An extended structural strength scaling law that captures the transition from the micrometer-scale FPZ through millimeter-scale yielding zone (YZ) to large-scale structures which follow linear elastic fracture mechanics (LEFM) is derived and then applied to analyze the effect of σ_{xx}. Presented here are the gap tests of aluminum alloy, in which three different levels of σ_{xx} are applied to scaled notched four-point-bend beams of depths D = 12, 24, 48 and 96 mm. Using an extended size effect law for plastic-hardening metals, it is found that, at crack-parallel stress $\sigma_{xx} \approx -40\%$ of the yield strength, the critical J-integral value gets roughly quadrupled, not only because of the well-known enlargement of the hardening YZ whose width is of millimeter scale, but also because of the increase of the FPZ width of micrometer scale. These results can be reproduced neither by line crack models, including the LEFM, cohesive crack and phase-field models, nor by peridynamic and various nonlocal models that ignore the tensorial nature of the material stress at the crack tip. The crack band models, being able to represent an FPZ of finite width and a YZ whose size evolves depending on σ_{xx}, can capture the effect of crack-parallel stresses provided that a realistic 3D tensorial damage constitutive model is used. Here, Bai–Wierzbicki's model is shown to capture the σ_{xx} effect on the G_f and J_{cr} qualitatively.

* Corresponding author.
E-mail address: z-bazant@northwestern.edu (Z.P. Bažant).

https://doi.org/10.1016/j.jmps.2023.105222
Received 30 October 2022; Received in revised form 1 January 2023; Accepted 21 January 2023
Available online 10 February 2023

1. Introduction

Fracture of polycrystalline plastic-hardening metals is an important engineering problem whose study has a long history (Anderson, 1991; Pineau et al., 2016a,c,b). Among many advances, the HRR theory developed by Hutchinson (1968b) and Rice and Rosengren (1968) became pivotal. This theory led to further important studies of the size of the hardening yielding zone (YZ, typically about 10 mm wide) and its relation to the material fracture energy (Betegón and Hancock, 1991; Xia et al., 1993; Gao et al., 1996). The interaction of the YZ with the normal component, σ_{xx}, of crack-parallel stress in the crack direction, usually called the T-stress, has been heavily studied since the 1990s (Anderson, 1991; O'Dowd and Shih, 1991, 1992).

These studies showed that the magnitude of the load that drove the crack propagation, applied in the transverse y-direction, had a close connection with the level of constraint at the crack tip, which varied for different test configurations. In a preceding study (Nguyen et al., 2021), an energetic size effect law was derived for the scaling of strength of plastic-hardening metallic structures with long notches or long cracks grown stably before the maximum load. This scaling law represents a generalization of the classical energetic scaling law of Type 2, obeyed by all quasibrittle materials, such as concrete, rocks, coarse ceramics, fiber composites, rigid foams, wood, sea ice or bone (Bažant, 1984b; Bažant et al., 1987; Bažant and Kazemi, 1991; Bažant and Planas, 1998; Dönmez, 2021a,b; Bažant et al., 2021).

The energetic size effect law, experimentally verified for concrete in 1987, Bažant et al. (1987) was first generalized to plastic-hardening materials by size effect tests of aluminum alloy (Bažant et al., 1987), but without detection of the intermediate asymptote and its theoretical basis. This asymptote, which bridges the micrometer scale of FPZ embedded within the YZ to the decimeter scale larger than the YZ, was formulated in the preceding 2021 study.

It must also be emphasized that the term "size effect" in materials science refers to a different physical phenomenon—the Hall-Petch law (Hall, 1951) which describes the dependence of the material yield strength on the size of polycrystalline grains in metals, and is explained by the arrest of dislocation lines at crystal boundaries.

The preliminary results from Nguyen et al. (2021) and Bažant et al. (2022) are here extended to determine how the strength scaling law is changed by a complex stress state at the crack tip. The gap test (Nguyen et al., 2020b,a) makes it possible to determine unambiguously the effect of the crack-parallel compressive stress, σ_{xx}, on material fracture energy G_f. This is best done by determining how σ_{xx} affects the size effect curve of nominal structure strength, σ_N. Such an effect was found to be significant, non-monotonic and strongly dependent on the loading path. Even though the stress-parallel crack effect is tested and numerically validated only for σ_{xx}, which acts in the propagation direction, the model is sufficiently calibrated to predict the effect of the out-of-plane normal and shear components, σ_{zz} and σ_{xz}. It shows that they can be equally important (see Nguyen et al. (2020a)). Note also that the material fracture energy G_f applies only to specimens sufficiently larger than the YZ, at which G_f coincides with the critical J-integral.

In the standard fracture test specimens, the stresses σ_{xx} (or T-stress), σ_{zz}, σ_{xz} parallel to the crack plane (x, z) are zero or negligible (x is the crack propagation direction). Yet, this is not the case in most practical situations. The main reason why the effect of crack-parallel stresses on fracture growth has been dismissed for so long is the fact that a crack is usually regarded as a plane, with a front of zero width, in which case σ_{xx} could have no effect. In reality, the crack becomes a plane (normally rugged) only at the end of fracture process. But what matters is the damage zone at the fracture front during crack growth. For every crack it has a finite width w_f (Nguyen et al., 2020b,a). This is the basic feature of the 1979 blunt crack model (Bažant and Cedolin, 1979) and the 1983 crack band model (Bažant, 1993; Bažant and Oh, 1983). Yet, experiments showed already in 1979 that, if w_f is finite, the effect of $\sigma_{xx}, \sigma_{zz}, \sigma_{xz}$ ought to be significant and that the damage tensor in the FPZ must play a role. This also means that the pointwise energy dissipation at the crack tip of Griffith cracks and the scalar stress–displacement law of the (fictitious) cohesive crack are incomplete and often insufficient characterizations of fracture. Rather, the cohesive law would have to be different for every possible stress state and every load path that leads to it. The role of the crack-parallel stress in concrete has long been suspected by a few investigators (Tschegg et al., 1995; Bažant and Cedolin, 1979; Bažant, 1993; Bažant and Oh, 1983), but a simple unambiguous test was lacking until the development of the gap test in 2020 (Nguyen et al., 2020b,a).

Here we begin with a brief review of the mathematical formulation of the scaling laws presented in the preceding study (Nguyen et al., 2021), which is needed for evaluating the gap test. This is followed by a generalization of these scaling law to capture the transitions between different regimes. The effect of the crack parallel stress σ_{xx} on the YZ is also updated to include other crack-parallel stress components (restricted, though, to fracture mode I). The changes in the size effect are studied experimentally on aluminum alloy over a broader range of crack-parallel compressive stress σ_{xx}, compared with Bažant et al. (2022). Then these generalized size effect formulations are used to deduce the effect of σ_{xx} on the material fracture energy, J_{cr}, and on the effective radius r_p of the YZ. The effect of σ_{xx} on the scaling asymptotes is also clarified. It should be noted that the range of specimens sizes considered here is much greater than the inhomogeneity size, which is the size of the polycrystalline grains (about 2 to 50 μm for aluminum alloy 6061 (Shankar et al., 2005; Zhang et al., 2018)). The asymptotes that are related to the sizes of YZ and FPZ can only be revealed by numerical modeling.

2. Fracture in plastic-hardening metal

2.1. Power-law stress–strain relation for plastic-hardening materials

Plastic-hardening metals can be satisfactorily described by the Ramberg and Osgood (1943) uniaxial stress–strain law (Fig. 1a,b):

$$\frac{\epsilon}{\epsilon_y} = \frac{\sigma}{\sigma_y} + \alpha_p \left(\frac{\sigma}{\sigma_y}\right)^n \tag{1}$$

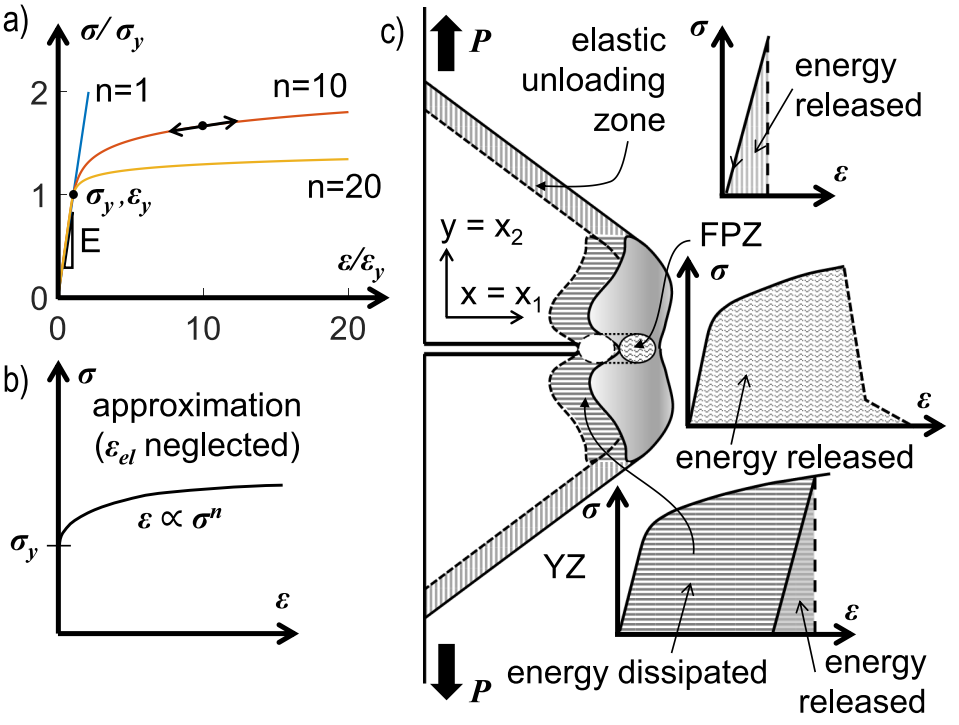

Fig. 1. (a) Stress–strain behavior of plastic-hardening metals and response curves for different hardening exponents n; (b) Approximation with the elastic strain neglected; (c) The release of energy density of material points in different zones (the yielding zone shape is computed for the gap test configuration).

where ϵ_y = initial yield strain, σ_y = initial yield stress; α_p = empirical parameter (usually denoted as α, but α is the standard notation for the dimensionless crack length); and n = plastic hardening exponent, typically 3 to 20 (Rice and Rosengren, 1968; Hutchinson, 1968b). The metal is considered plastically incompressible by volume, which means that it can yield only in shear. This allows us to deal solely with deviatoric stress and strain tensors, s_{ij} and e_{ij}.

For analysis it is advantageous that the aforementioned range of exponent n leads to such a large plastic deformation that the elastic strain can be neglected by comparison, as assumed in the Hutchinson–Rice–Rosengren (HRR) theory (Hutchinson, 1968b; Rice and Rosengren, 1968). One merit of the power law in Eq. (1) is that the stress–strain law becomes self-similar with respect to the strain or stress magnitude. Together with the separated nature of the power-law singularity (demonstrated in Bažant et al. (2021) and Nguyen et al. (2021)), the asymptotic near-tip deformation field becomes self-similar with respect to radial affine transformations, which makes an analytical solution feasible. The tensorial generalization of the uniaxial stress–strain law is assumed to be of von Mises form (Anderson, 1991; Hutchinson, 1968b; Rice and Rosengren, 1968; Kanninen and Popelar, 1985):

$$\frac{\epsilon}{\epsilon_y} = \alpha_p \left(\frac{\sigma}{\sigma_y}\right)^n \tag{2}$$

$$\text{and} \quad e_{ij} = \frac{3\alpha_p \epsilon_y}{2\sigma_y}\left(\frac{\sigma_{ef}}{\sigma_y}\right)^{n-1} s_{ij} \quad \text{where} \quad \sigma_{ef} = \sqrt{\tfrac{3}{2} s_{kl} s_{kl}} \tag{3}$$

Here the initial yield stress and strain in uniaxial tests, σ_y and ϵ_y, must be understood as the equivalent, or effective, yield limit parameters indicating the point where the power law for strain takes off; see Fig. 1a; σ_{ef} is the scalar effective stress (possible higher-order terms such as $\sigma_{ef}^{(3)} \propto s_{km} s_{mn} s_{nk}$ are omitted, and the summation rule for repeated numerical cartesian subscripts ($m, n, k = 1, 2, 3$) is implied). The use of the deformation theory of plasticity in HRR and in the J-integral is a simplifying assumption, but Hutchinson and Paris (Hutchinson and Paris, 1979) showed it to be rather accurate in this problem.

2.2. Large-scale yielding in small structures with a restricted yielding zone

Consider first the specimens so small that the YZ (Fig. 2) occupies all of the cross section and its size may get restricted by, or interact with, the boundaries. We analyze geometrically similar specimens of different sizes D, with similar notches or cracks. It was found in Hutchinson (1968b), Rice and Rosengren (1968) and Nguyen et al. (2021) that the near-tip fields of displacement u_i, deviatoric stress s_{ij}, and deviatoric strain e_{ij} have separated forms which may be written as:

$$u_i = \alpha_p \epsilon_y r_p (r/r_p)^{mn+1} F_i(\theta) \tag{4}$$

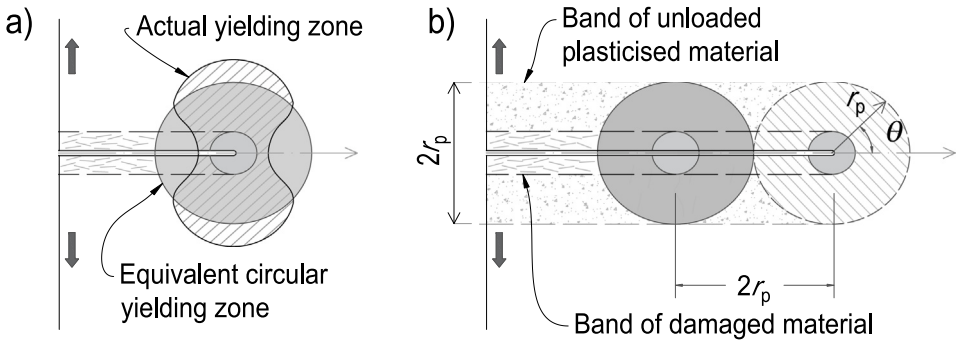

Fig. 2. (a) Actual and equivalent YZs with the same virtual work (or volume); (b) Displacement of the equivalent YZ and FPZ as crack propagates.

$$e_{ij} = \alpha_p \epsilon_y (r/r_p)^{mn} \varphi_{ij}(\theta) \tag{5}$$

$$s_{ij} = \sigma_y (r/r_p)^{m} \psi_{ij}(\theta) \tag{6}$$

$$\text{where} \quad \varphi_{ij}(\theta) = \tfrac{3}{2}\psi_{ij}(\theta)\left(\tfrac{3}{2}\psi_{kl}(\theta)\psi_{kl}(\theta)\right)^{(n-1)/2} \tag{7}$$

Here (r, θ) are the polar coordinates centered at the crack tip, with angle θ measured from the crack extension line, exponent m is a constant and r_p is the effective size (or radius) of the YZ, both to be determined later (Fig. 2a). The dimensionless angular functions F_i, ψ_{ij} and φ_{ij} represent the solutions of ordinary differential equations which can be approximately calculated by the finite difference method (Rice, 1968b; Nikishkov, 1998) or finite element method (Levy et al., 1971), or conformal mapping (Revil-Baudard et al., 2018; Xin et al., 2010). Note that if the elastic strains were not neglected, the above-mentioned separated fields would still be valid but only asymptotically, close enough to the tip.

The energy flux passing through the YZ into the FPZ is given by Rice's J integral (Rice, 1968a):

$$J = \int_\Gamma \left(\overline{W}\mathrm{d}y - \nu_j\, s_{ij} u_{i,1} \mathrm{d}s\right), \quad \overline{W} = \int s_{ij}\mathrm{d}\epsilon_{ij} \tag{8}$$

where Γ is a closed contour around the crack tip, s is the contour length coordinate, ν_i is the unit outward normal of the contour, $y = x_2$, $\partial_1 = \partial/\partial x_1$; $\overline{W}$ is the nonlinear strain energy density. The rate J is meant with respect to the crack length a, not time. The material is considered nonlinearly elastic, as if the unloading would follow the same curve as elastic loading. Therefore, the J-integral is path-independent provided that the J contour avoids the unloading zone in the wake of the YZ.

Conveniently we choose a circular J-integral path, for which $\mathrm{d}s = r\mathrm{d}\theta$ and $\mathrm{d}y = r\mathrm{d}\theta\cos\theta$. From this and from Eqs. (4)–(6), we find the radial dependence of the first term of J-integral, $\int_{-\pi}^{\pi} \overline{W}\mathrm{d}y \propto r^m r^{mn} r = r^{m(n+1)+1}$ (where $\propto$ is the proportionality sign). For the second term of J integral we find the same, i.e., $\int_{-\pi}^{\pi} \nu_j s_{ij} u_{i,1}\mathrm{d}s \propto r^m r^{mn+1} r^{-1} r = r^{m(n+1)+1}$ (see also Appendix I of Nguyen et al. (2021)). To satisfy the condition of path-independence of J, the exponent of r must vanish, i.e., $m(n+1)+1 = 0$. Hence,

$$\boxed{m = -\frac{1}{n+1}} \tag{9}$$

as shown in 1968 by Rice and Rosengren (1968) and Hutchinson (1968b). Note that, in the limit case of elastic behavior, $n = 1$, Eq. (9) would give $m = -1/2$, as it must. Also note that the requirement $s_{ij}e_{ij} \propto 1/r$, shown in 1968 (Rice and Rosengren, 1968; Hutchinson, 1968b), is satisfied. Eq. (9) does not apply to perfect or near perfect plasticity ($n \to \infty$), but a separate solution for this case was given by Hutchinson (1968a).

From Eqs. (9) and (4)–(6) for large-scale yielding in relatively small structures, one can derive the scaling laws (see Eqs. 5.3.10 in Kanninen and Popelar (1985)):

$$u_i = \alpha_p \epsilon_y r_p (r/r_p)^{\frac{1}{n+1}} F_i(\theta) \tag{10}$$

$$e_{ij} = \alpha_p \epsilon_y (r/r_p)^{-\frac{n}{n+1}} \varphi_{ij}(\theta) \tag{11}$$

$$s_{ij} = \sigma_y (r/r_p)^{-\frac{1}{n+1}} \psi_{ij}(\theta) \tag{12}$$

It became customary to characterize the structure strength in terms of the nominal structure strength, $\sigma_N = P/bD$, which is a load parameter with the dimension of stress; P is the applied load, b is the structure width (for a two-dimensional structure), and D is the characteristic structure size, measured on geometrically similar structures at homologous locations. Evidently, for small enough structures with large-scale yielding and a fully plasticized cross section, $\sigma_N \propto s_{ij}$ and $r \propto D$, and so Eq. (12) yields the scaling law:

$$\boxed{\sigma_N \propto \sigma_y \left(\frac{r_p}{D}\right)^{\frac{1}{n+1}}} \quad \text{(for large-scale yielding)} \tag{13}$$

where the proportionality constants are omitted as irrelevant to the size effect. Note that, in the limit of $n \to 1$, this scaling law becomes $\sigma_N \propto D^{-1/2}$, as known for LEFM. Eq. (13) is needed as an anchor for asymptotic matching of the broad-scale size effect law.

2.3. The release of energy in different zones

Consider now a specimen large enough so that its YZ is entirely surrounded by a linearly elastic zone. The strain energy density $\overline{W}$ of the nonlinearly elastic material imagined to approximate the plastic-hardening YZ is

$$\overline{W} = \int s_{ij} \mathrm{d}e_{ij} \tag{14}$$

The right-hand side of Eq. (12) for s_{ij} must be multiplied by a loading parameter, μ. To match it, the right-hand side of Eq. (11) must then be multiplied by μ^n, and the expression for $\mathrm{d}e_{ij}$ must be multiplied by $n\mu^{n-1}$. Integration from $\mu = 0$ to $\mu = 1$ then leads to the energy density:

$$\overline{W}(r,\theta) = \alpha_p \sigma_y \epsilon_y \varphi_{ij}(\theta)\psi_{ij}(\theta)(r_p/r)n/(n+1) \tag{15}$$

When the crack length extends along with the advancing YZ, a part of the structure is getting unloaded. The elastic strain energy density, $\overline{W}_e$, may be small in the YZ but significant in the elastic unloading zone. Taking into account only the deviatoric stresses and strains, we have the elastic energy density $s_{ij}s_{ij}/2G$. Substitution of $G = \sigma_y/\epsilon_y$ for the elastic shear modulus into Eq. (6) gives the strain energy density at point (r,θ) of the YZ:

$$\overline{W}_e(r,\theta) = \tfrac{1}{2}\sigma_y \epsilon_y (r_p/r)^{2/(n+1)} \psi_{ij}(\theta)\psi_{ij}(\theta) \tag{16}$$

The irreversible part of the energy of the YZ gets dissipated by material unloading in the wake of YZ (via dislocations, stacking faults or grain boundary microcracking). All this energy gets fully dissipated when the YZ advances by the distance $2r_p$ (Fig. 2b). Hence, the rate of energy dissipation from the YZ is:

$$G_p = \frac{1}{2r_p}\int_{-\pi}^{\pi}\int_0^{r_p} [\overline{W}(r,\theta) - \overline{W}_e(r,\theta)] r \,\mathrm{d}\theta \,\mathrm{d}r = \sigma_y \epsilon_y \, r_p Q_p \tag{17}$$

$$\text{where} \quad Q_p = \frac{n\alpha_p}{2(n+1)}\int_{-\pi}^{\pi} \varphi_{ij}(\theta)\psi_{ij}(\theta)\mathrm{d}\theta - Q_e \tag{18}$$

Similarly, all of the elastic strain energy of the YZ, which is calculated based on the elastic stiffness, gets fully released once the YZ advances by $2r_p$ (see Fig. 1c). So the contribution of the elastic energy is:

$$G_e = \frac{1}{2r_p}\int_{-\pi}^{\pi}\int_0^{r_p} \overline{W}_e(r,\theta) r \,\mathrm{d}\theta \,\mathrm{d}r = r_p \, \sigma_y \epsilon_y \, Q_e \tag{19}$$

$$\text{where} \quad Q_e = \frac{n+1}{8n}\int_{-\pi}^{\pi} \psi_{ij}\psi_{ij} \,\mathrm{d}\theta \tag{20}$$

It should be noted that $J_{cr} \propto r_p$ and $Q_p, Q_e \propto \mu^2$, μ being the loading parameter (see Appendix C).

3. Scaling of structures of hardening plastic materials — summary and updates

3.1. Size effect based on a constant yielding zone

Here, a physical analogy of quasibrittle structures may be utilized, as in Nguyen et al. (2021). The energy release rates $\mathcal{G}_s$ and $\mathcal{G}_b$ arise from two different zones: (1) $\mathcal{G}_s$ is the rate (with respect to a, not time) of energy release from the unloading elastic zone of the structure, which is approximately proportional to D (for $D \to \infty$), and (2) $\mathcal{G}_b$ is the rate of energy release in the FPZ wake of the damage band which does not depend on D as the band is initially under transverse tension proportional to σ_N.

Unlike quasibrittle materials, in which there is no plastic yielding, a plastic-hardening YZ develops between the elastic zone and the damage zone of FPZ. In this section, we only consider the first two zones. The fully developed YZ (typically of millimeter dimensions) plays three physical roles: (1) it conveys energy flux J (with no energy loss, as proven by path-independence of J-integral) through the YZ to the crack tip; (2) it dissipates energy as the material deforms plastically; and (3) when its wake unloads, the strain energy that was initially stored in the band of width $2r_p$ before the YZ arrived, independent of D, is released at a rate $\mathcal{G}_b$. Hence, the balance of energy rates requires that:

$$\boxed{\mathcal{G}_s + \mathcal{G}_b = J_{cr}} \tag{21}$$

For $\mathcal{G}_b$ we can use a constant characteristic length, analogous to c_f, equal to the equivalent size of the yielding band, r_p; so $\mathcal{G}_b = (\sigma_N^2/E')\, g_0' r_p$. For $\mathcal{G}_s$ we can use the same definition as for a quasibrittle material, i.e., $\mathcal{G}_s = (\sigma_N^2/E')Dg_0$. Substituting the terms contributing to the energy release rate, we get the condition of energy conservation:

$$\frac{\sigma_N^2}{E'} Dg_0 + \frac{\sigma_N^2}{E'} g_0' r_p = \mathcal{G}_s + \mathcal{G}_b \tag{22}$$

Upon solving for σ_N, we obtain the size effect law for fracture of plastic-hardening metals:

$$\boxed{\sigma_N = \frac{\sigma_0}{\sqrt{1 + D/D_0}}} \tag{23}$$

This size effect law has the same form as the SEL of quasibrittle structures (Appendix A, Eq. (59)). Its coefficients, though, are expressed differently:

$$\sigma_0^2 = E' J_{cr}/g_0 D_0, \quad D_0 = g_0' r_p/g_0 \tag{24}$$

The asymptotes of this law are also the same as for the SEL:

$$\sigma_N \underset{D \to 0}{\Rightarrow} \sigma_0 = \text{constant}, \quad \sigma_N \underset{D \to \infty}{\Rightarrow} D^{-1/2} \tag{25}$$

The size effect on structure strength is the quintessential characteristic of all fracture behavior, the plastic-hardening metals included, and the size effect method is an unambiguous way to determine the fracture energy and estimate the FPZ or YZ size. For the size effect law (23) to apply to metals, r_p must, of course, remain approximately constant through various structure sizes. This is confirmed in Fig. A.1 by finite element (FE) results for different sizes, based von Mises plasticity. The effective size r_p roughly represents the radius of a circle having approximately the same area as the fully developed YZ, provided that the boundary is at least at distance $1.5r_p$ from the crack tip and the structures of different sizes reach about the same value of J-integral (this value may best be computed by the equivalent domain integral (Rice, 1968a; Li et al., 1985) using the finite element method (FEM)).

Calculations show that r_p remains approximately constant through different structure sizes except when the size is too small. Despite the irregular shape of YZ (Fig. A.3) this distance normally suffices for the YZ not to touch the boundary. The approximate constancy of r_p is nevertheless not universal, and the crack-parallel stress affects r_p.

Similar to the original quasibrittle energetic size effect law (Appendix A), Eq. (23) can be rearranged as linear regression:

$$Y = AX + C \quad \text{where} \quad X = D, \quad Y = 1/\sigma_N^2 \tag{26}$$

$$A = 1/\sigma_0^2 D_0, \quad C = 1/\sigma_0^2 \tag{27}$$

Fitting these equations to test data, one can identify the fracture energy J_{cr}, as well as the effective width $2r_p$ of the YZ. To do so, one needs only the maximum loads for specimens of sufficiently different sizes (this allows dispensing with postpeak softening measurements, even though they are known to greatly help accuracy in the case of concrete). After determining the value of g_0 (and E'), a linear regression of the measured (X, Y) values furnishes A and C. As a result, $\sigma_0 = 1/\sqrt{C}$ and $D_0 = C/A$. Finally, the fracture energy of the structure can be computed as:

$$J_{cr} = g_0/E' A, \quad r_p = g_0 C/g_0' A \tag{28}$$

3.2. Size effect based on yielding zone restricted by the structure boundary

When the structure size is not large enough, being such that the distance from the notch to the boundary in the x-direction is less than the size of the fully developed YZ, we have a transition from small-scale yielding to large-scale yielding, and a restricted YZ size must be considered. Denote this size as $D = 2r/\tilde{h}_0$ where $\tilde{h}_0 = \tilde{h}(\alpha_0)$ and $\tilde{h}(\alpha)$ is a dimensionless function depending on the geometry of the specimen and the hardening power, and $2r$ is the diameter of an equivalent annular structure. Similar to Eq. (12), $s_{ij} \propto \sigma_N$ and $2r$ is replaced by $h_0 D$, we can write $\sigma_N = \sigma_y (2r_p/\tilde{h}_0 D)^{\frac{1}{n+1}}$, where r_p is supposed to be the effective radius of the YZ if such a zone is allowed to fully develop (as if it were not restricted by the boundary). Therefore,

$$2r_p = (\sigma_N/\sigma_y)^{n+1} \tilde{h}_0 D \tag{29}$$

The linear elastic strain energy that was initially stored in the material and was subsequently released by the passage of the YZ is, per unit length in the x-direction, obtained by replacing G_b in Eq. (22);

$$\mathcal{G}_b = \frac{\sigma_y^2}{E'} \left(\frac{\sigma_N}{\sigma_y} \right)^{n+1} h_0 D \tag{30}$$

where h_0 is a function of $\tilde{h}_0$ and the plastic-hardening constants. Note that we use σ_y^2/E' instead of σ_N^2/E' to express the correspondence between the fully developed YZ size and its equivalent elastic energy density. Using $2r = \tilde{h}_0 D$, we can also derive G_b from Eqs. (11)–(12) and $\sigma_y^2/E'(\sigma_N/\sigma_y)^{n+1}$ can be interpreted as the energy density scaled with the real structure size D. Substituting this equation into the energy balance Eq. (21), one gets:

$$\boxed{\frac{\sigma_y^2}{E'} \left(\frac{\sigma_N}{\sigma_y} \right)^2 g_0 D + \frac{\sigma_y^2}{E'} \left(\frac{\sigma_N}{\sigma_y} \right)^{n+1} h_0 D = J_{cr}} \tag{31}$$

Again, this equation differs only by the second term from Eq. (22). We may rewrite it as follows and then solve it numerically:

$$AX^{n+1} + BX^2 = C \qquad \text{in which} \tag{32}$$

$$A = h_0 D, \quad B = g_0 D, \quad C = E' J_{cr}/\sigma_y^2, \quad X = \sigma_N/\sigma_y \tag{33}$$

Alternatively, the procedure described in Nguyen et al. (2021) leads to an approximate, yet rather accurate, closed-form scaling law:

$$\boxed{\sigma_N = \sigma_0 \left[\left(D/cD_0 \right)^{\sqrt{2/(n+1)}} + \left(D/D_0 \right)^{\sqrt{(n+1)/2}} \right]^{-1/\sqrt{2(n+1)}}} \tag{34}$$

where

$$c = g_0/h_0;\ \ \sigma_0 = \sigma_y,\ \ D_0 = E' J_{cr}/\sigma_y^2 g_0 \tag{35}$$

As $n+1 > 2$, the power of the first term in the brackets will be smaller than that of the second term. Based on this observation, the asymptotes of this scaling law can be written:

$$\sigma_N \underset{D \to 0}{\Rightarrow} D^{-1/(n+1)}, \quad \sigma_N \underset{D \to \infty}{\Rightarrow} D^{-1/2} \tag{36}$$

The fracture energy and the effective radius of the YZ, which is what sets the length scale, can then be computed:

$$J_{cr} = \sigma_y^2 g_0 D_0/E', \quad r_p = g_0 D_0/2 \tag{37}$$

3.3. The scaling law of the transition from micrometer to millimeter-scale structures

Polycrystalline metals have a simpler microstructure than concrete and most quasibrittle materials. However the scaling of their strength is more complicated. While the damage zone of concrete, about 0.5 m in size, is surrounded by an elastically unloading material, in metals a large hardening YZ is inserted between the damage zone and the elastic zone. Being of millimeter dimensions (when fully developed), it is three orders of magnitude larger than the width of the damage zone, which is of micrometer dimensions and represents the FPZ.

So far we considered the scaling law when only the YZ and the elastic unloading zone are present. In this section, we consider a structure of several to a hundred micrometer dimensions, in which the distance to the structure boundary is only few times larger than the FPZ. We note that the damage in the FPZ of metals and alloys (except for special cases such as the embrittlement caused by the hydrogen absorption along the grain boundaries) stems from the void formation due to the mismatch between polycrystal grains, excessive dislocation, and coalescing point defects (voids). In any case, these defects accumulate within a damage softening volume near the crack tip. We assume that the extent (nominal size) of this volume remains approximately constant when the structure is geometrically scaled.

The energy release rate in Eq. (21) may be rewritten in terms of $\mathcal{G}_b$ and $\mathcal{G}_h$, the latter of which gives the energy release rate from the FPZ. Due to the foregoing assumption, we use a constant characteristic length scale c_f. The emergence of this term is due to the expansion of the energy release rate of the HRR field (in which $a = a_0 + c_f$):

$$\frac{\sigma_y^2}{E'} D h(\alpha) \left(\frac{\sigma_N}{\sigma_y} \right)^{n+1} = G_f; \quad \text{where} \quad h(\alpha) \approx h(\alpha_0) + h'(\alpha_0) \frac{c_f}{D} \tag{38}$$

$$\Rightarrow \frac{\sigma_y^2}{E'} h_0 D \left(\frac{\sigma_N}{\sigma_y} \right)^{n+1} + \frac{\sigma_y^2}{E'} h_0' c_f \left(\frac{\sigma_N}{\sigma_y} \right)^{n+1} = \mathcal{G}_b + \mathcal{G}_h = J_{cr} \tag{39}$$

After solving for σ_N, a new size effect law emerges:

$$\boxed{\sigma_N = \sigma_0 \left(1 + D/D_0 \right)^{-1/(n+1)}} \tag{40}$$

The form of this law is similar to the SEL for quasibrittle structures (Appendix A, Eq. (59)), except for the power. Its parameters and asymptotes are:

$$\sigma_0 = \sigma_y \left(E' J_{cr}/\sigma_y^2 h_0' c_f \right)^{1/(n+1)}, \quad D_0 = c_f h_0'/h_0 \tag{41}$$

$$\sigma_N \underset{D \to 0}{\Rightarrow} \sigma_0 = \text{constant}, \quad \sigma_N \underset{D \to \infty}{\Rightarrow} D^{-1/(n+1)} \tag{42}$$

The relevant fracture properties can then be computed:

$$J_{cr} = \mathcal{G}_b + \mathcal{G}_h = \left(\frac{\sigma_0}{\sigma_y} \right)^{n+1} \frac{\sigma_y^2 h_0 D_0}{E'}, \quad c_f = h_0 D_0/h_0' \tag{43}$$

3.4. Three asymptotic scaling regimes

As a consequence of Eqs. (23), (34), (40), the combined scaling law consists of two transitions between three power-law asymptotes appearing as straight lines in the logarithmic-scale plot of strength versus size. An intermediate asymptote (in the sense of Barenblatt (1979)) is inserted between the horizontal small-size asymptote for damage in the FPZ and a large-size asymptote of slope $-1/2$ for linear elastic fracture mechanics (LEFM); see Fig. 3. Thus we need to consider the size effects for:

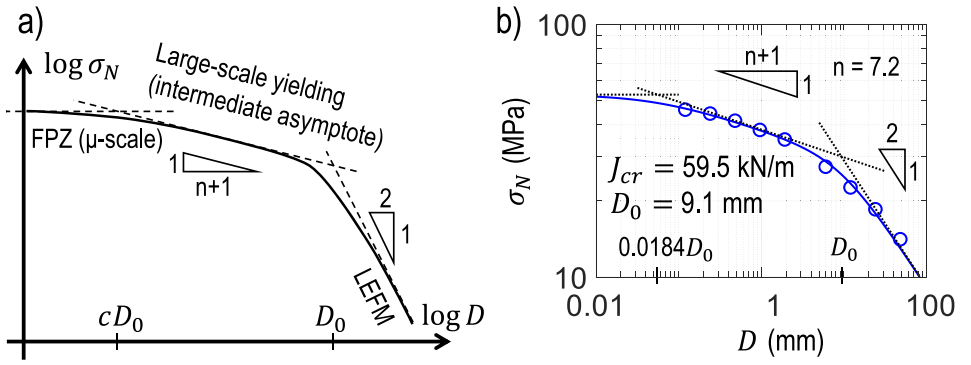

Fig. 3. (a) Three-asymptotic scaling law to describe fracture of plastic-hardening polycrystalline metals and (b) its validation based on Bai–Wierzbicki's model (Bai and Wierzbicki, 2010). Two length scales are separated by the ratio between the FPZ and YZ sizes, which is $c = 0.0184$.

(1) the transition from the small-size asymptote to the intermediate asymptote, which applies to large-scale yielding in relatively small specimens in which the YZ size is restricted by the boundaries;

(2) the transition from the intermediate asymptote, which applies for small-scale yielding in relatively large specimens, to the large-scale asymptote for LEFM; and

(3) the direct transition from damage to LEFM, which skips the intermediate asymptote and applies only to specimens much larger than the YZ.

The combined scaling law can be expressed by an equation formally identical to Eq. (34) except for a different meaning of c:

$$\sigma_N = \sigma_0 \left[\left(1 + D/cD_0\right)^{\sqrt{2/(n+1)}} + \left(D/D_0\right)^{\sqrt{(n+1)/2}} \right]^{-1/\sqrt{2(n+1)}} \tag{44}$$

The three asymptotes of this law are:

$$\sigma_N \underset{D \to 0}{\Rightarrow} \sigma_0 = \text{constant}, \tag{45}$$

$$\sigma_N \underset{D \gg cD_0 \text{ and } D \ll D_0}{\Rightarrow} D^{-1/(n+1)}, \tag{46}$$

$$\sigma_N \underset{D \to \infty}{\Rightarrow} D^{-1/2} \tag{47}$$

Here c, in contrast to (34), represents the approximate ratio of the FPZ size to the fully developed YZ size. In quasibrittle materials, due to the nonexistence of the plastic-hardening YZ, the first and the third regimes dominate and the second regime disappears. The fracture characterizing properties can then be calculated from:

$$J_{cr} = \sigma_0^2 g_0 D_0 / E', \quad r_p = g_0 D_0 / g_0', \quad c_f = c r_p \tag{48}$$

The transition of the nominal strength between asymptotes in Eq. (44) when the structure size D increases reflects the characteristics of the dominating volume at each structure size. The scaling law will reduce to the original type 2 SEL in quasibrittle materials if the second asymptote vanishes, which corresponds to the disappearance of the YZ that delimits the elastic zone and the FPZ.

Since experimental results of the energetic size effect of microscale metallic structures are unavailable, the data to validate the scaling law in Eq. (44) have been generated numerically using the damage constitutive law developed by Bai and Wierzbicki (2008) and Bai and Wierzbicki (2010).

Three-dimensional finite-strain simulations having the same geometry as in Nguyen et al. (2021) were used. The element sizes at the crack front were chosen to be the same as the grain size of polycrystal (the rationale behind the selection is discussed later). The same element size was used for all geometrically scaled structures, in accordance with Bažant and Oh (1983). The parameters of the constitutive law and the fitting of the material characterization tests are presented in Appendices E and F.

Although the Bai–Wierzbicki model contains no length scale, the fracture energy value is implied by using finite elements of a size equal to the material characteristic length l_0. As indicated in Bažant and Planas (1998) and Bažant and Oh (1983), l_0 is typically equal to one to just a few grain sizes (Bažant, 1984a). Its proper value is best obtained from the transitional size in size effect experiments. If a larger element size has to be used, one may (with some loss of accuracy) tune the dissipated energy value so that the energy dissipated per element remain approximately the same. However, for this study, the same element size has always been used in the crack-front region for specimens of different sizes D.

To generate consistent numerical results for the scaling law, the initial notch width was taken to be the same for all the different structure sizes. Fig. 3 demonstrates a good fit of the numerical results to Eq. (44), and thus reveals the scale separation in the aluminum alloy tested.

Even though the size of the plastic-hardening YZ must be, and is, independent of the element size, the FPZ size in the crack band model is not. In fact, the phenomena that cause softening within the FPZ, i.e., the voids nucleation and coalescence at the grain boundaries and the excessive cumulative dislocation density, are always associated with an intrinsic length scale. For example, the grain size in a polycrystalline solid will determine the distance between the growing voids (see the discussion of the grain in Appendix G).

The front diameter of the notch was ≈600 μm (Fig. A.2a), which is one order magnitude greater than the finite element size. This might be thought to be excessive, but FE studies show it is not, for the present analysis based on large crack growth in the size effect tests. True, the notch needs to be very sharp for observing the initial crack growth, as in R-curve testing or in fatigue growth initiation. But what matters here is that the notch tip is narrow compared to the YZ. After large crack growth within a large YZ, as in postpeak response, what matters is the crack tip rather than the notch tip. The fracture energy for initial crack growth would, of course, change with the notch width, in the same manner as it does for alumina A.2b. However, this will not alter the present conclusions whose main focus is the effect of the externally applied crack-parallel stress on the fracture energy.

4. Effect of crack-parallel stress

So far, we have only considered scaling laws based on the effective size of the YZ and the characteristic size of the FPZ, yet their attributes have not been discussed. Many authors (O'Dowd and Shih, 1991, 1992; Xia et al., 1993; Gao et al., 1996) showed that a stress (σ_{xx}) parallel to the crack plane and proportionally increasing with the load had a significant effect on the R-curve and on the J_{cr} of metals and alloys through its effect on the YZ. In addition, Nguyen et al. (2020b) and Nguyen et al. (2020a) showed that a constant parallel stress of different levels would modify the size of the FPZ of quasibrittle materials non-monotonically. It is, therefore, necessary to determine the effective size of YZ, r_p, and the characteristic size of the FPZ, c_f, as functions of σ_{xx}, σ_{zz}, σ_{xz}.

4.1. Crack-parallel stress effect on the yielding zone size

Up to the second term of the LEFM near-tip asymptotic expansion (Williams, 1952), the elastic near-tip field of σ_{ij} is

$$\sigma_{ij}^{el} = (K_I/\sqrt{r}) f_{ij}(\theta) + T_{11}\delta_{i1}\delta_{j1} + T_{33}\delta_{i3}\delta_{j3} + T_{13}\left(\delta_{i1}\delta_{j3} + \delta_{i1}\delta_{j3}\right)/2 \tag{49}$$

where T_{ij} = field of uniform normal stress parallel to the crack plane; $f_{11}(\theta) = \cos\frac{1}{2}\theta(1 - \sin\frac{1}{2}\theta\sin\frac{3}{2}\theta)/\sqrt{2\pi}$, and $f_{13}, f_{23} = 0$ (Bažant and Planas, 1998, p.86); $K_I = \sqrt{E'G_f}$ = mode I stress intensity factor; $E' = E$, $T_{33} = 0$ for plane stress and $E' = E/(1-\nu^2), T_{33} = \nu T_{11}$ for plane strain (ν = Poisson ratio, E = Young's modulus); $T_{13} = 0$ in both 2D cases. The stress field is computed using the modified boundary layer method based on an imagined circle containing the entire plasticized volume. This formulation is appropriate for small-scale yielding in which the σ_{ij}^{el} field prevails at sufficiently large r. For small r, the near-tip singular plastic-hardening field is given by Eq. (6) :

$$\sigma_{ij}^{pl} = \sigma_y (r/r_p)^{-\frac{1}{n+1}} \psi_{ij}(\theta) \tag{50}$$

The size and shape of the YZ bordering on the outer elastic stress field is complicated, as illustrated in Fig. 2a. For a scaling law spanning several orders of magnitude of structure size, it suffices to have a rough estimate of the effective radius r_p of this plastic-hardening YZ. Although the precise size and shape of this zone is not important for the global behavior, they need to be considered to calculate r_p. As proposed by Hutchinson and Rice, one needs to determine r_y as the r-value at which the equivalent stress is equal to σ_y (Anderson, 1991), while the elastic stresses in the outer field and the and plastic-hardening stresses in the inner field are in overall force equilibrium (Hutchinson, 1968b; Kanninen and Popelar, 1985). The equilibrium should properly be considered for different angles θ, each of which gives a different r_y, and one must either choose one characteristic angle θ (usually $\theta = 0$) or conduct some sort of averaging over all θ to get a unique r_p.

Another matching method was proposed in 2021 in Nguyen et al. (2021). It uses the virtual work equivalence to identify the optimal r_p for which the inner and outer stress fields are in equilibrium. This virtual work equivalence is imposed to find a new effective radius r_p' at which equilibrium is attained. We set

$$r_p' = r_p\zeta \tag{51}$$

where parameter ζ is identified from a virtual equilibrium equation ensuring the resultants of the elastic and plastic stresses in the propagation direction x_1 to be equal, i.e.,

$$\int_{-\pi}^{\pi}\int_0^{r_p'} \sigma_{11}^{el}\, r\, \mathrm{d}\theta\, \mathrm{d}r = \int_{-\pi}^{\pi}\int_0^{r_p'} \sigma_{11}^{pl}\, r\, \mathrm{d}\theta\, \mathrm{d}r \tag{52}$$

Substituting Eqs. (49) and (50), integrating and rearranging Eq. (52), we obtain:

$$r_p' = \boxed{\zeta r_p = \frac{\kappa\, l_0}{(1 - \eta T_{11}/\sigma_y)^2}} \quad \text{where} \tag{53}$$

$$l_0 = \frac{E'G_f}{\sigma_y^2}, \quad \kappa = \left(\frac{C_e}{C_nC_p}\right)^2, \quad \eta = \frac{\pi}{C_nC_p} \tag{54}$$

$$C_n = \frac{n+1}{2n+1}, \quad C_p = \int_{-\pi}^{\pi} \psi_{11}(\theta)\,\mathrm{d}\theta, \quad C_e = \frac{2}{3}\int_{-\pi}^{\pi} f_{11}(\theta)\,\mathrm{d}\theta \tag{55}$$

where $l_0 = K_{Ic}^2/\sigma_y^2$ = Irwin's material characteristic length and the other constants are dimensionless.

More accurately. one could take into account all the stress components by means of a J_2-equivalent stress;

$$\int_{-\pi}^{\pi}\int_{0}^{r'_p}\left[\left(\sigma_{11}^{el}-\sigma_{22}^{el}\right)^2+\left(\sigma_{22}^{el}-\sigma_{33}^{el}\right)^2+\left(\sigma_{33}^{el}-\sigma_{11}^{el}\right)^2+6\sigma_{12}^2\right]^{1/2} r\,\mathrm{d}\theta\,\mathrm{d}r \;= \tag{56}$$
$$\int_{-\pi}^{\pi}\int_{0}^{r'_p}\left[\left(\sigma_{11}^{pl}-\sigma_{22}^{pl}\right)^2+\left(\sigma_{22}^{pl}-\sigma_{33}^{pl}\right)^2+\left(\sigma_{33}^{pl}-\sigma_{11}^{pl}\right)^2+6\left(\sigma_{12}^2+\sigma_{13}^2+\sigma_{23}^2\right)\right]^{1/2} r\,\mathrm{d}\theta\,\mathrm{d}r$$

Unlike Eq. (52), the effective size r'_p would then depend on T_{11}, T_{33} and T_{13}. But the estimate of r'_p would not change significantly.

Note that we neglect here the effects of plate thickness, expected to be minor. One is the "wall effect" related to the size of the inhomogeneities (Bažant, 1996). It could matter only if the thickness of the specimen was of a similar size range as the grains in polycrystalline metal, which is on the order of a few micrometers. The second is the plastic "shear lip" (Krafft et al., 1961). The third is the 3D singularity at the intersection of the crack front edge with the plate surface, which requires the crack front edge to terminate at the boundary at a certain angle at which the singularity is of the $(-1/2)$-power law type if the crack propagates (Bažant and Estenssoro, 1979). However, the effect of the nonuniform stress state across the thickness must be accounted for, which leads to a non-zero σ_{zz} arising at the crack tip (as discussed in the next section). The apparent fracture energy is therefore defined by the fracture energy measured in the thickest specimens (Anderson, 1991).

4.2. Historical distinction between intrinsic and extrinsic crack-parallel stresses

Depending on the geometry, some loads generate, according to elasticity, non-zero nonuniform crack-parallel T-stresses. They are nonuniform and proportional to the load μ, and we call them "intrinsic" in this study to distinguish them from the "extrinsic" ones which are applied externally. Their effect, called stress triaxiality, was first studied in 1991 by O'Dowd and Shih (1991) and O'Dowd and Shih (1992), using a modified boundary analysis. Due their spatial variation, interpretation of their effect on fracture is ambiguous. Zhu and Leis (2006), Lu and Meshii (2014), Narasimhan and Rosakis (1990) and Zehnder and Rosakis (1990) showed that, in general, the bending configurations suffered from the intrinsic T-stresses less than the tensile ones. The notch-to-depth ratio of the specimens also played a key role. For each of several structure sizes, the magnitude of intrinsic T_{11}-stress generated at the maximum load was compared with the extrinsic value and we concluded that the notch-to-depth ratio of 0.33 generated a negligible intrinsic T-stress ($\approx 5\%$ of the extrinsic T_{11}), see Fig. 4a. This is in line with the conclusion in Lu and Meshii (2014). The proportionality between the intrinsic T-stresses and the nominal strength is usually called by the biaxiality ratios, i.e., $T_{11}\sqrt{\pi a}/K_I$ and $T_{33}\sqrt{\pi a}/K_I$.

While the intrinsic T_{11}-stress is negligible in the gap test configuration, the intrinsic T_{33}-stress is not. As shown in Figs. 4b–c, T_{33}-stress is negative and its magnitude increases with decreasing b/D. This is due to the fact that the material points closer to the mid-plane of the specimen experience a plane-strain stress state while those closer to the free surfaces are under plane stress. Therefore, the greater the thickness b of the specimen, the larger the zone exhibiting higher stress triaxiality. Although the maximum value of this stress can be as high as −200 MPa (Fig. 4b), the averaged value over the entire YZ remains small, except when $b/D < 0.2$ (Fig. 4c) for which there is a significant deviation from the plane-strain condition as plane-stress develops (Larsson and Carlsson, 1973; Lv et al., 2018). This behavior leads to a deviation from the assumption of constant r_p (Fig. 4d) and to a significant change of the size and shape of the YZ. The effect of these intrinsic T-stresses on the size of the YZ was carefully studied in Zhu and Leis (2006), Kirk and Dodds (1992), Yeh et al. (2006), Miao et al. (2017), Sobotka and Dodds (2011), Matvienko (2014) and Matvienko (2015). A three-dimensional scaling of the gap test as well as the three-point bend and compact tension tests, in which b/D would be kept constant, would alleviate the aforementioned problems.

The approximate constancy of r_p in Figs. 4d and A.1 (when $D \leq 48$ mm at $b = 10$ mm) is important for the validity of the scaling laws in Eq. (23), (34), (40), (44).

Note that for quasibrittle materials, in which the YZ is absent, the effect of the intrinsic T-stresses is negligible. This is important not only for the original gap tests of concrete (Nguyen et al., 2020b,a) but also for the latest gap tests of the cross-ply fiber composites (Brockmann and Salviato, 2022).

5. Gap tests of aluminum alloy 6061-T651

The "intrinsic" crack-parallel stresses that arise and proportionally increase with the crack-driving load have been considered, but only for the specimen geometries used in standard testing. These stresses, sometimes referred to as crack-tip constraints, have been shown to significantly affect the material fracture energy. Yet, their effect was investigated only by numerical simulations (Larsson and Carlsson, 1973; Miao et al., 2017; Gupta et al., 2015; Liu et al., 2019; Yuan and Brocks, 1998) or via indirect experiments (Hancock et al., 1993; Joyce and Link, 1995; Shen et al., 2005). In these experiments, the intrinsic stresses vary during loading and can be altered only by changing the specimen geometry and loading configuration. Such experiments have been difficult to interpret unambiguously.

The advantage of the gap test is that it yields easily interpreted unambiguous results and is simple to carry out. For a description of its experimental setup and loading apparatus, see Nguyen et al. (2020b) and Nguyen et al. (2020a). Briefly, the end supports of a standard notched three-point bend beam are installed with suitable gaps and, next to the notch, the specimen is supported by elastic

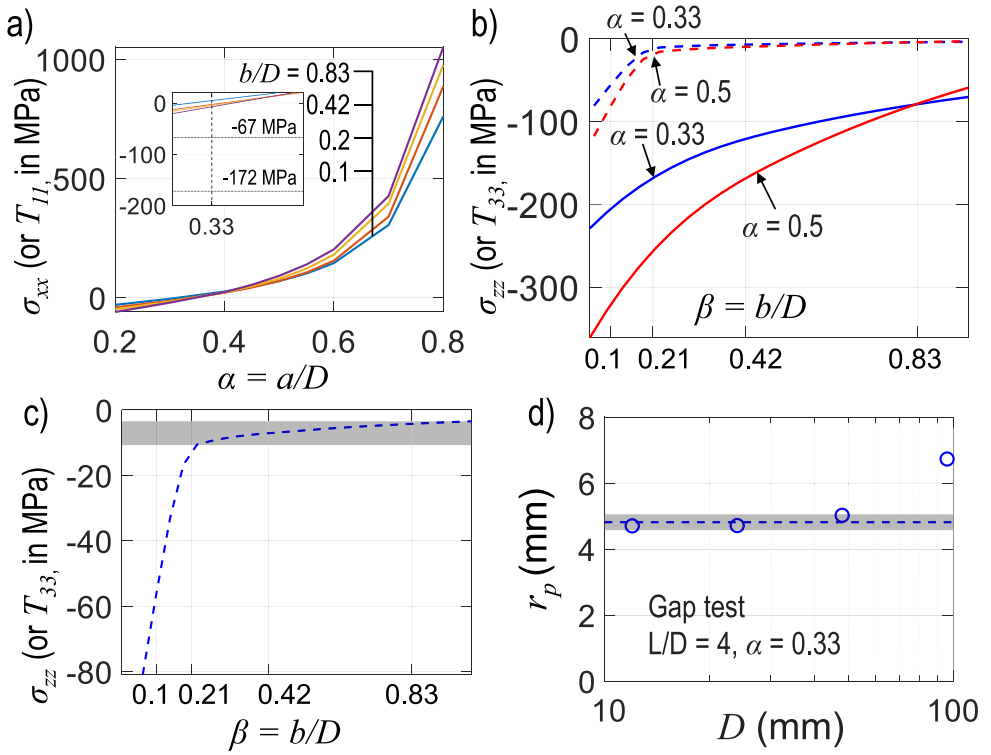

Fig. 4. (a) The dependence of intrinsic σ_{xx} (or T_{11}) on the notch-to-depth and thickness-to-depth ratios, i.e., $\alpha = a/D$ and $\beta = b/D$. (b) The dependence of intrinsic σ_{zz} (or T_{33}) on α and β; the solid curves represent the stress value at mid-plane and at a radial distance of $r = 0.5$ mm from the tip and the dashed curves represent the stress value averaged over the entire YZ. (c) The averaged σ_{zz} value remains small when $D < 50$ mm, which results in a small variation (< 5%) of the effective YZ size r_p (d). When $D > 50$ mm, the YZ size significantly deviates from the constancy assumption.

perfectly-plastic pads (Nguyen et al., 2020a, Fig. 3). Under vertical load at midspan, the pads first generate a field of crack-parallel compressive stress σ_{xx}, which is almost uniform near the notch tip. When the pads begin yielding, under nearly constant load, the end gaps close (Nguyen et al., 2020b, Figs. 1a-c) and then the end reactions begin applying a bending moment, which causes mode I fracture growth at the crack tip. For evaluation it is advantageous that the load-support system is statically determinate, both before and after the gaps close while the pads yield.

Another advantage is that one can apply the size effect method (Bažant and Kazemi, 1991; Nguyen et al., 2021) to determine the fracture energy, J_{cr}, and the size of the inelastic zone, either YZ or FPZ. To this end, the tests must be carried out on specimens of distinctively different sizes, preferably, though not necessarily, geometrically scaled. The gap test has originally been applied to concrete (Nguyen et al., 2020b,a). Soon it was extended to fiber composite (Brockmann and Salviato, 2022) (gap tests of shale and fiber-reinforced concrete are also underway). The limited preliminary gap tests of aluminum mentioned in Bažant et al. (2022) have now been extended and are reported here.

Polypropylene pads of the right shape and cross section were found to yield at the stress level comparable to the compressive strength of concrete (Nguyen et al., 2020b,a). However, in the present tests of aluminum alloy 6061-T651, the supporting pads were made of polyvinyl-chloride (PVC) and pure copper (Cu), which sufficed to achieve constant crack-parallel stresses of 14.4% and 38.6% yield strength of the tested aluminum alloy. To characterize their basic properties, these three elasto-plastic materials were tested according to the ASTM standards—E9-19 for Al and Cu, and D695-15 for PVC. Fig. 5a shows the stress–strain results of the cylindrical specimens with diameter $2r = 20$ mm and height $H = 60$ mm for Al and Cu, and $2r = 15$ mm and $H = 30$ mm for PVC. The strain rates were 0.005 mm/s for the metals, and 0.0008 mm/s for the PVC. The deformed shapes are shown in Fig. 5b. The plastic buckling and bulging seen in the figures occurred after the peak load, which is irrelevant for the gap test.

Additional compression tests of Cu and PVC were carried out on specimens of the same shape as the pads used. The stress–strain curves recorded are shown in Fig. 5c,d for the PVC and Cu. The plastic plateaus of the pad materials, required for the crack parallel stress levels in the notched Al beams, were −67 MPa and −172 MPa. Since the yield strength of Cu, 355 MPa, is much higher than 172 MPa, the average stress in the pads had to be reduced. This was achieved simply by drilling holes in the Cu pad, as seen in Fig. 5d.

The single-edge notched beam specimens of aluminum, scaled geometrically in 2D with constant aspect ratio of 1:4 and notch-to-depth ratio of 0.33, and with the same width of 10 mm, are shown in Fig. 6a,b. Their depths are 12, 24, 48 and 96 mm. Fig. 6c,d show the results of standard three-point bend tests (with no gaps, no pads). A specimen of one size, as deformed in postpeak softening,

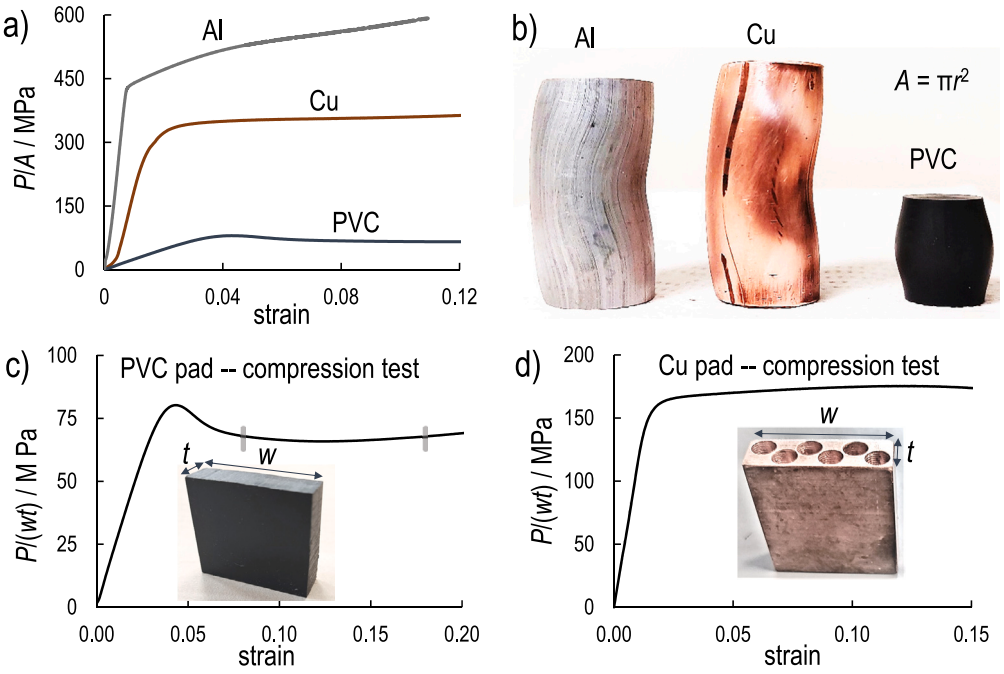

Fig. 5. (a) Uniaxial stress–strain curves of aluminum (Al), copper (Cu) and polyvinyl-chloride (PVC); (b) The deformed shapes of Al, Cu and PVC loading pads after compression test; (c,d) compression tests of PVC pad and perforated Cu pad.(Note: w and t are the cross sectional dimensions and r is the radius.)

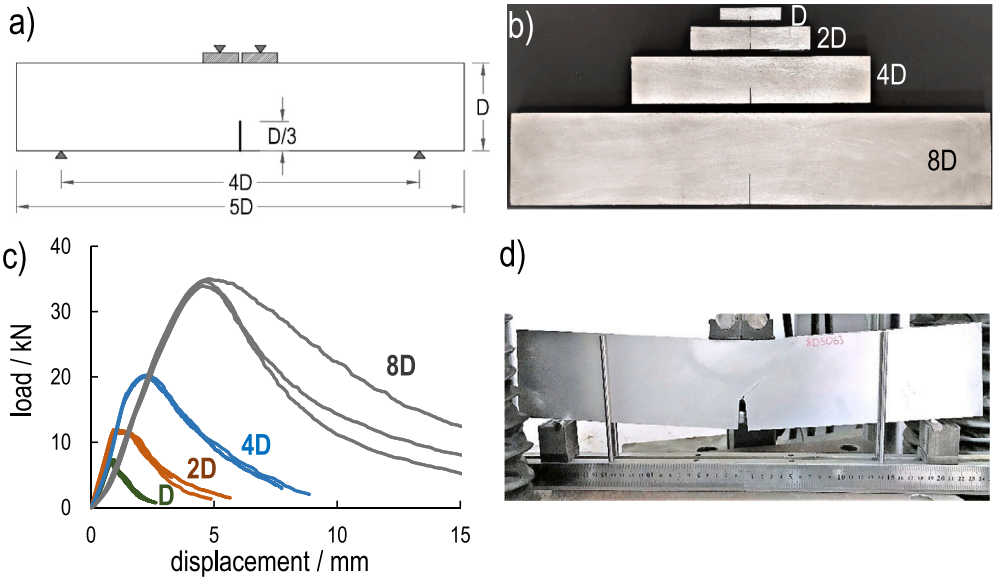

Fig. 6. (a) The geometry of the Al specimens used; (b) Geometrically similar specimens of four scaled sizes; (c) The load–deflection curves of the scaled specimens; (d) Failure and grown crack image in 8D sized specimen.

is seen in Fig. 6d. It is restrained by stiff vertical straps to prevent lateral buckling. In smaller specimens the buckling restraint was unnecessary.

Stronger supports against lateral buckling had to be used in the specimens with pads, as seen in Figs. 7a and 8a on the left. On the right, one can see 8 recorded load–deflection curves with Al and Cu pads, generating compressive crack-parallel stresses −67 MPa and −172 MPa. The second rising portions of the curves represent the effect of the bending moments after the gaps at beam ends have already closed (the initial convex curvatures are due to gradual seating of the pads or beam end supports, which must be disregarded).

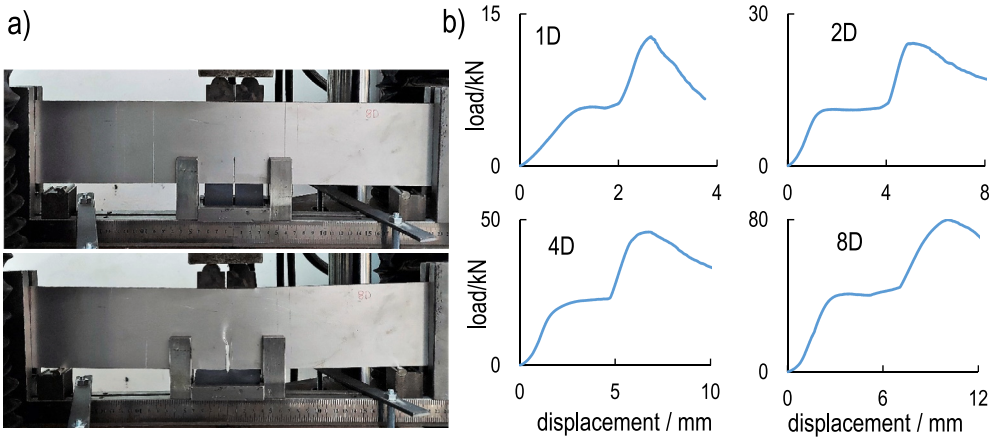

Fig. 7. (a) The loading scheme of the gap tests using PVC pads and corresponding failure and cracking; (b) The load–deflection curves of the gap tests using PVC pads generating a 67 MPa crack-parallel compression in the Al specimens.

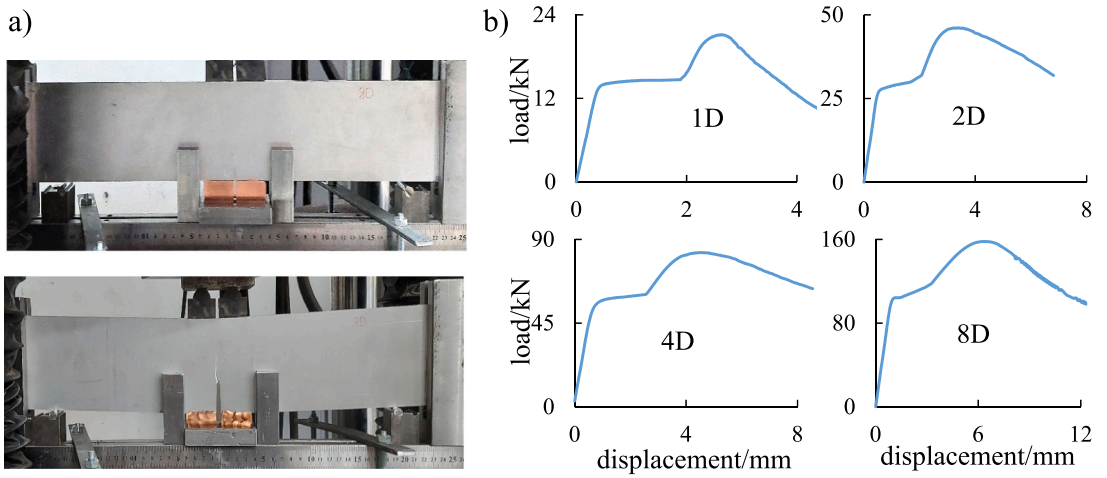

Fig. 8. (a) The loading scheme of the gap tests using Cu pads. and the corresponding failure and cracking; (b) The load–deflection curves of the gap tests using Cu pads that generate a 172 MPa crack-parallel compression in the Al specimens.

Ideally, a near-horizontal plateau controlled by the pads should have developed on these curves before reaching the "hill" with the second rise of load. Such a plateau, unfortunately, has not been attained for all the load–displacement curves; see Figs. 7–8. Rather, a small rise was observed in these cases, yet it was taken into account in post-processing so that the real peak loads could be extracted (repeating these tests with bigger gaps or with pads of different types, so as to achieve a plateau, was not possible). But note that what really matters is the stress of the pads at the peak load (hidden below the "hill"). Though not identifiable from these diagrams, a baseline yield behavior was extrapolated by FEM. The validity of this evaluation is supported by the systematic trend of the results plotted in Fig. 9a,b. The post-mortem analysis showed no evidence of shear lip.

6. Results of gap tests of aluminum and their discussion

The data points in Fig. 9 show the measured peak nominal stress values σ_N for scaled gap tests of 4 different sizes $D = 12, 24, 48, 96$ mm, and for 3 different levels of crack-parallel stress levels (σ_{xx} was plotted as a ratio of the yield strength σ_y and the compression was shown as negative values). The 3 solid curves in Figs. 9a–b represent the optimal fits of the data points with the scaling laws in Eqs. (23) and (34), respectively. Note the systematic trends of the data points. Also note that the structures with $D = 96$ mm were omitted due to the low b/D ratio (hence a large negative σ_{zz}). These structures therefore had a larger YZ (see Fig. 4d) and their peak loads were typically higher than the fitted size effect curves (see data points marked by × in Fig. 9). For the three stress levels, the coefficients of variation of regression errors (defined as the root-mean-square error divided by data mean) are 9.7%, 1.5% and 6.2%, which is quite low. The fact that these trends are so systematic lends credence to our assumption that the lack of visible plateau in Fig. 8 did not spoil the results significantly.

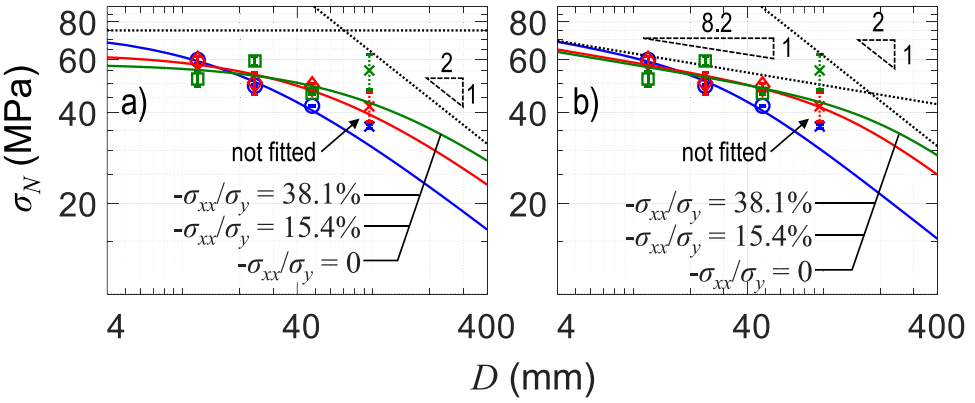

Fig. 9. (a) The fitting of the scaling law in Eq. (23) against experimental data of aluminum with different structure sizes D at three different crack-parallel stress levels σ_{xx}/σ_y; (b) ditto, but Eq. (34) is used instead.

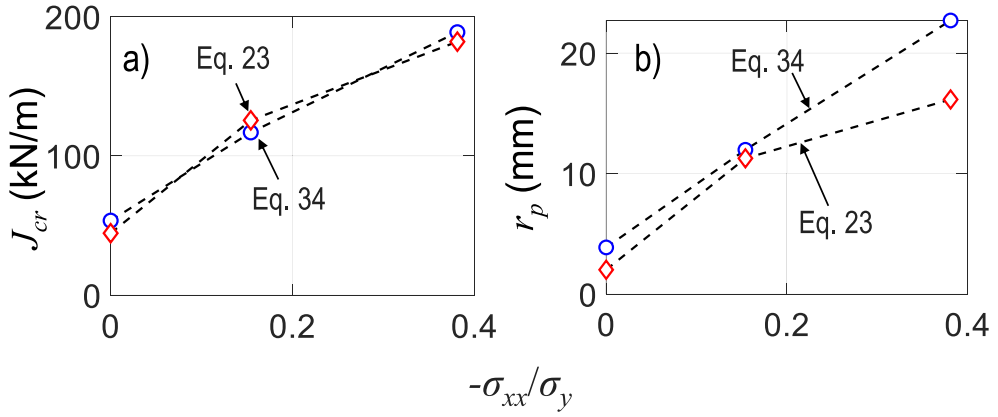

Fig. 10. The variation of (a) fracture energy and (b) the effective size of YZ with crack-parallel stress σ_{xx}.

Further note in Figs. 9a–b that the LEFM size effect slope of $-1/2$ is still far from being attained, even for the largest specimens. This means that a much larger size would be needed for the material to follow the LEFM (i.e., to attain the small-scale yielding range, see Appendix B). Also note that what determines the fracture energy J_{cr} is the position of the LEFM asymptote of slope $-1/2$, which is marked by a dashed line for each curve. The shift of the asymptote to the right means an increase of J_{cr}. Obviously, these asymptotes for the three levels of σ_{xx} are shifted relative to each other (Fig. 9), which means that the J_{cr} values for different σ_{xx} are quite different (Fig. 9). The extension of the $-1/(n+1)$ asymptote to the right (due to the increase of the transition size D_0) indicated an enhancement of ductility of the aluminum alloy.

Figs. 9a and b show the same test results for two different scaling laws. The fracture energy values obtained from the fitting of these two equations are plotted in Fig. 10 for the three levels of crack-parallel stress σ_{xx} used in the tests. The closely matched fracture energy from these fittings implied that their underlying assumptions were both valid at the chosen size range. However, when σ_{xx} increased, the YZ might grow larger than the ligament length of the specimens, leading to a deviation of the computed r_p between these equations. However, in this case, r_p obtained from Eq. (34) is more reliable as it does not hinge on the assumption of small-scale yielding.

The enhancement of J_{cr} and r_p with increasing crack-parallel compression σ_{xx}, as seen in Figs. 10a–b, is remarkably strong, stronger than for concrete. The J_{cr} value at $\sigma_{xx} = 0$ is ≈ 51 kN/m perfectly matches the one measured in Nguyen et al. (2021) and is confirmed by J-integral for the same material. A major part of this enhancement is due to the effect of σ_{xx} (or T-stress) on the YZ of a millimeter-scale width, which has been well known since the 1980s (Gao et al., 1996; O'Dowd and Shih, 1991, 1992). The question is if any portion of this enhancement may be due to the interaction of σ_{xx} with the micrometer-scale FPZ, which is embedded within the YZ. Doubtless the FPZ has a finite width of micrometer dimensions, several times larger than the crystal size (but still 3 orders of magnitude smaller than the YZ).

A noteworthy point is that the size effect curves in Fig. 9a and b cross each other, and the effect of σ_{xx} gets reversed at the small size limit (as also marked in Fig. 11a). The reason is that the small size asymptotic limit of the size effect law is a crack filled by a perfectly plastic material, which may be reasonably described by the Mohr or von Mises yield envelope; see Fig. 11b. On the

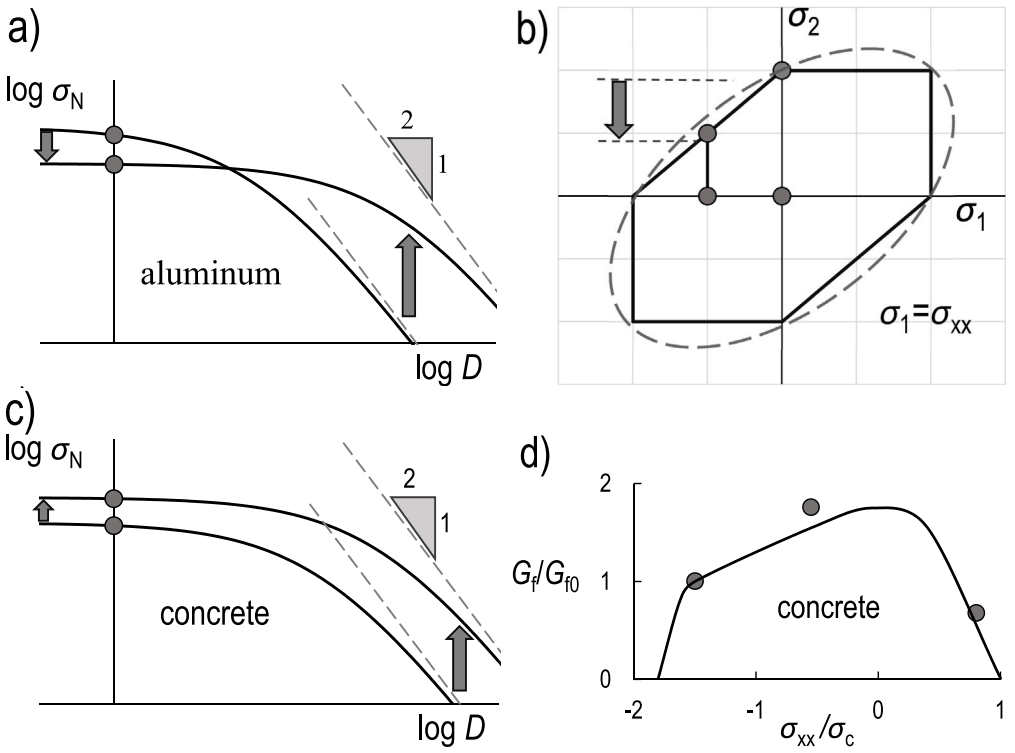

Fig. 11. (a) Size effect curves of aluminum in logarithmic scales for $\sigma_{xx} = 0$ and for large σ_{xx} ($= T$); (b) Mohr and von Mises yield envelopes of metals; (c) size effect curves of concrete, showing, for comparison, that for quasibrittle materials the curves do not cross; (d) dependence of J_{cr} on σ_{xx} in concrete, and the optimum fit by crack band model with microplane M7 constitutive law.

envelope, one can see that increasing the magnitude of compression, $|\sigma_1|$, causes a drop in the transverse principal stress, $\sigma_2 = \sigma_{yy}$, which controls the small-size asymptote. This, of course, only applies to the blunt notch case.

A comparison with concrete is instructive. Fig. 11d shows the diagram of the dependence of J_{cr} of concrete on σ_{xx}/f_c recently obtained experimentally (Nguyen et al., 2020b,a) (here σ_c = compression strength of concrete in the beam specimens). At the compression limit, $\sigma_{xx} = \sigma_c$, this diagram drops to a zero fracture energy. Could the same behavior be expected for aluminum? Probably not. Although no tests for $|\sigma_{xx}| > 0.4\sigma_y$ have been conducted for aluminum, the diagram of J_{cr} versus σ_{xx} should end at the yield limit $|\sigma_{xx}| = \sigma_y$ with a significant value of J_{cr}.

Another difference is seen in the size effect curves. For concrete, these curves, shown in Fig. 11c, do not cross on approach to the small-size limit, unlike those for aluminum. Again, the reason is that in concrete, at the uniaxial tensile strength limit, no yielding plateau due to plastic material bridging the crack exists, regardless of the size.

7. Numerical validations and predictions of crack-parallel stress effect

Bai and Wierzbicki (2008) and Bai and Wierzbicki (2010) developed a constitutive damage law for metallic materials based on the fracture initiation in specimens tested under biaxial and triaxial stress states (Bao and Wierzbicki, 2004). These tests were later revisited and extended in Papasidero et al. (2015). Due to the claimed capability of capturing the fracture behavior under various proportional and non-proportional stress states, this law has been selected to assess the effect of crack-parallel stresses on the fracture energy of aluminum allow.

7.1. Numerical validations and the effect of σ_{xx}

The variation of the YZ as a consequence of various σ_{xx} (and σ_{zz}) was numerically documented in Sobotka and Dodds (2011), Lu and Meshii (2014) and Matvienko (2014) using high-resolution finite element simulations and the interaction integral (Nakamura and Parks, 1992). In those simulations, refined element sizes were used at the crack front, along with the Gurson–Tvergaard constitutive law (Gurson, 1977; Tvergaard, 1989). The present numerical simulations have been designed in a same manner as the size effect tests in Fig. 3, except for differences in the geometry. Similar to Sobotka and Dodds (2011), Lu and Meshii (2014) and Matvienko (2014), Fig. 12a shows an increasing trend as the compressive σ_{xx}-stress increases. This also agrees with the trend observed in the experiments, yet at a lower stress, level. The enlargement of the r_p of simulated YZ, due to increase of σ_{xx}, was more

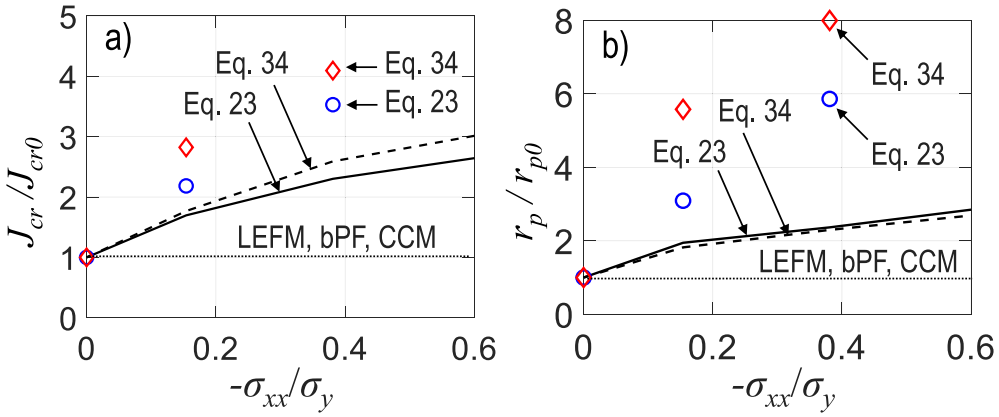

Fig. 12. A comparison of the experimental and numerical simulations based on the constitutive law in Bai and Wierzbicki (2010) reveal a moderate enhancement of (a) the fracture energy and (b) the effective size of YZ with extrinsic crack-parallel stress σ_{xx}.

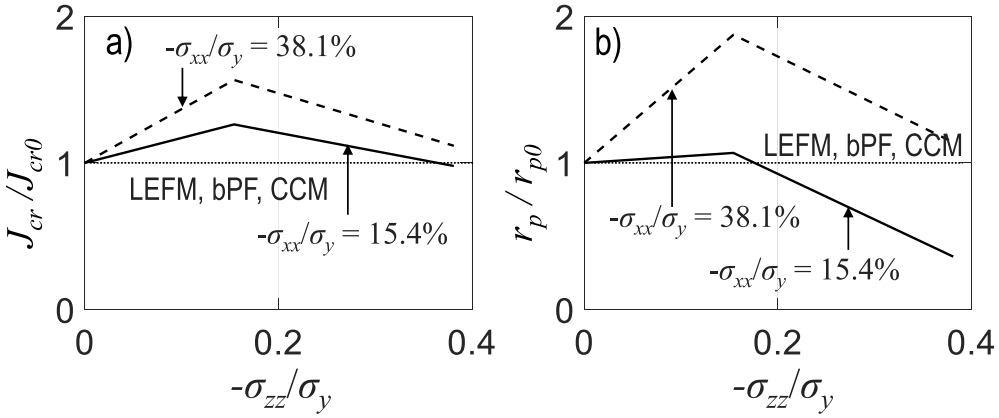

Fig. 13. The dependence of (a) the fracture energy and (b) the effective size of YZ on extrinsic crack-parallel stress σ_{zz} predicted by the constitutive law in Bai and Wierzbicki (2010).

moderate (see Fig. 12b). In these simulations, the constitutive model was calibrated to match the uniaxial tension and compression tests of cylindrical specimens and the fracture energy measured on geometrically scaled beams made of the selected aluminum alloy at zero crack-parallel σ_{xx} (i.e., at zero"extrinsic" T-stresses).

To clarify the change of YZ for various σ_{xx}/σ_y ratios, Fig. A.3 shows a sketch of the boundary of YZ at mid-plane of the specimen with size $D = 24$ mm for $\mathcal{G} = J_{cr}$, which is the boundary of the plastically deforming zone. The results show that the YZ increases in size as the ratio σ_{xx}/σ_y becomes negative and decreases as it becomes positive. However, the reduction in size of the YZ was less significant in magnitude than the expansion. Moreover, Fig. A.3 shows a larger change in the FPZ size measured transversely to the crack (y-direction) compared to that measured in parallel, which is expected due to slips on inclined planes caused by axial compression. This effect is path-dependent (Benzerga et al., 2012; Nguyen et al., 2020a). It requires a more accurate numerical model or a set of experiments with higher resolution (Kim et al., 2012).

7.2. Extrapolated predictions for the effect of transverse stress σ_{zz}

The same numerical model is now used to investigate the effects of σ_{zz} and of the combination of both applied stresses σ_{xx} and σ_{zz} on the fracture energy of aluminum alloy. Figs. 13 and A.4 show a non-monotonic trend of the fracture properties. This trend is neither confirmed nor disproved by previous studies. For example, based on Eq. (56) and a previous numerical study by Matvienko (2014) and Matvienko (2015), the YZ size must monotonically increase as σ_{zz} becomes negative. However, Lv et al. (2018) obtained the same non-monotonic trend of fracture energy using FEM. This may be explained by the excessive growth of the YZ in the z-direction while the extent of the elastic field bordering the YZ shrinks, which restricts the validity of the small-scale yielding assumption, Eq. (56). As almost the entire ligament length experiences excessive plastic deformation, void nucleation intensifies and may trigger crack growth. However, the inconsistency of model predictions calls for experiments to clarify the effect of σ_{zz} and, at the same time, for the development of a more accurate damage constitutive relation for the FPZ.

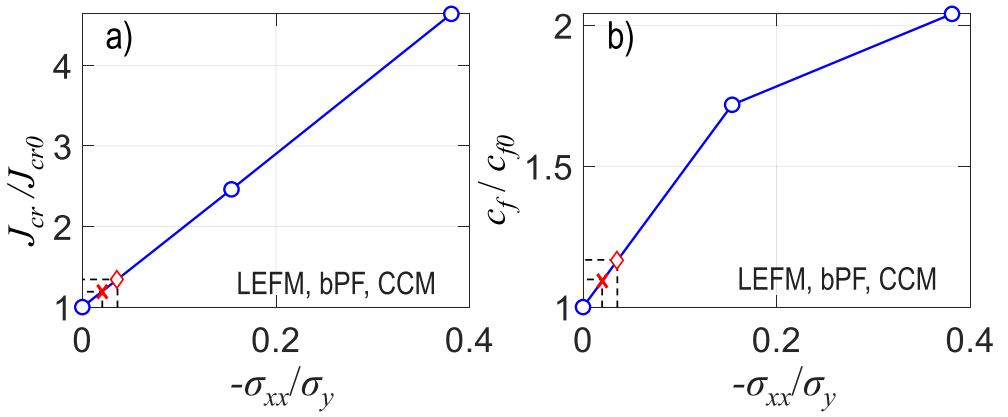

Fig. 14. The dependence of (a) the fracture energy and (b) the size of FPZ on extrinsic crack-parallel stress σ_{xx} predicted by the constitutive law in Bai and Wierzbicki (2010) (◇ and × represent the realistic σ_{xx} the element at the tip when $\sigma_{pad} = -15.4\%\sigma_y$ and $-38.1\%\sigma_y$).

7.3. The effect of σ_{xx} on the characteristic size c_f

To assess what part of the fracture energy gets dissipated within the micrometer-scale FPZ, we perform numerical simulations of the gap test with the structure sizes ranging from $D = 0.36 \rightarrow 5.76$ mm. We consider the same span-to-depth and notch-to-depth ratios, the same specimen thicknesses, and require the ligament length to be ≥3-times the element size, which allows the effect on the FPZ to get manifested. To avoid a blunt notch with its complications, a small fictitious notch of a width equal to one grain size of the polycrystal, taken as 40 μm, needs to be used, as shown in Fig. A.2. At this scale, neither the FPZ nor the YZ will dominate the crack front, and Eq. (40) for large-scale yielding needs to be used to extract the fracture energy from the scaling law.

The computation results shown in Figs. 14 and A.5 indicate that the fracture energy increases with increasing compression σ_{xx}. This is similar to concrete and shale, but opposite to cross-ply laminate (Brockmann and Salviato, 2022).

The trend observed in Fig. A.5 is, however, opposite to that observed for the small-size specimens shown in Fig. 9. We posit that this conflicting trend is a consequence of the sharpness of the notch. For the case of blunt notch (notch width is ≈15 times the grain size), the peak load is controlled mainly by the cohesive strength of the grain in front of the crack rather than the energy that flows into it. Therefore, a higher σ_{xx} will reduce the strength in y-direction, as explained by the Mohr circle in Fig. 11. However, for the case of sharp crack, the increase of $-\sigma_{xx}/\sigma_y$ will increase the nominal strength of the structures of various sizes in this range.

The sharpness of the notch has another consequence for the effect of σ_{xx}. If the notch is blunt, the actual stress σ_{xx} experienced by the material points within the FPZ is greatly reduced. In this case σ_{xx} is no longer $\approx \sigma_{pad}$ (see Fig. A.2), and so its real value is represented by the ◇ and × points in Fig. 14. Therefore, if the effect of σ_{xx} on the YZ and FPZ could be superposed, the YZ would contribute up to 25% of the total change of the fracture energy. In reality, though, the superposition assumption is too simplistic, and a revised scaling law using Eq. (44), and depending on the crack-parallel stresses, is required. But its development is beyond the scope of this paper.

8. Conclusions

1. The presence of the millimeter-scale yielding zone (YZ) bordering the micrometer-scale fracture process zone (FPZ) calls for a generalized size effect law for plastic-hardening structures, a law that describes the transitions between each two of the three subsequent asymptotes identified in the preceding study.
2. The slope of $-1/2$ in the log–log size effect plot is an indicator of the small-scale yielding regime, in which the linear elastic fracture mechanics is known to apply to metals. The present specimen sizes are not large enough to approach this asymptotic slope closely. One might see it as a disadvantage but it is actually an advantage because the effective YZ radius, r_p, can be identified only by testing in the transitional size range of intermediate asymptote, which dominates between the small-size and large-size asymptotes.
3. Extension of the previous gap tests of aluminum to three different levels of the crack-parallel compressive stress σ_{xx} provides clear evidence that σ_{xx} plays a significant role in the size effect.
4. Regression analysis of the gap tests of different sizes for the same σ_{xx} level yields unambiguous evidence that the crack-parallel stress, σ_{xx}, affects the fracture energy G_f, equal to J_{cr}. This is in addition to the well-known effect of σ_{xx} on the effective radius, r_p, of the YZ.
5. Increasing σ_{xx} from 0 to $0.4\sigma_y$ causes both J_{cr} and r_p to roughly quadruple. Although no tests were made at $|\sigma_{xx}| > 0.4\sigma_y$, the extension of the curve of J_{cr} versus σ_{xx} is expected not to tend to zero for $\sigma_{xx} \rightarrow -\sigma_y$ (i.e., the yield strength) because, in contrast to concrete, aluminum under compression yielding in x-direction still has undiminished tensile yield strength in the y-direction.

6. Compared to quasibrittle materials, the results of the gap test of aluminum are more systematic, with a lower scatter. This makes the evidence clearer.
7. Unlike quasibrittle materials such as concrete, the size effect curves of nominal strength of geometrically similar notched metallic specimens under various levels of crack parallel stress cross each other. Thus they produce at the small size asymptotic limit a reverse trend, such that the small-size asymptotic strength for high compression magnitude $|\sigma_{xx}|$ occurs at smaller σ_N.
8. The results show that, under the effect of compressive σ_{xx}, the FPZ accounts for 25% of the fracture energy enhancement while the remaining 75% is due to the increase of the YZ.
9. To reproduce the present experiments mathematically, an FPZ of correct finite width, described by a realistic tensorial damage constitutive model, must be used. The finite element crack band model can do that.

CRediT authorship contribution statement

A. Abdullah Dönmez: Conceptualized and designed research, Performed the experiments, Analyzed the data, Contributed to writing the paper. **Hoang T. Nguyen:** Conceptualized and designed research, Performed the simulations, Formulated the fitting equations, Analyzed the data, Contributed to writing the paper. **Houlin Xu:** Performed the simulations, Contributed to writing the paper. **Zdeněk P. Bažant:** Conceptualized and designed research, Conceived size effect analysis, Wrote the first draft, Contributed updates.

Declaration of competing interest

The authors declare that they have no known competing financial interests or personal relationships that could have appeared to influence the work reported in this paper.

Data availability

Data will be made available on request.

Acknowledgments

Funding under NSF, United States Grant No. CMMI-1439960 to Northwestern University is gratefully acknowledged. Partial support was also obtained under ARO, United States grant W911NF-19-1-0034, also to Northwestern. The first author also thanks to ITU BAP for the support under grant no 42833.

Appendix A. Derivation of classical scaling law for quasibrittle structures with no plasticity

To derive the scaling law for small-to-large scale transition of structure size, the approach used for quasibrittle materials needs to be reinterpreted and generalized (Bažant, 1984b; Bažant et al., 1987; Bažant and Kazemi, 1991; Bažant and Chen, 1997; Bažant and Planas, 1998; Bažant, 2005). We review it briefly here. The energy release rate of linear elastic fracture mechanics (LEFM) may be expressed as $\mathcal{G} = (\sigma_N^2/E')Dg(\alpha)$ where $\alpha = a/D$, D = characteristic structure size, a = crack or notch length, and $g(\alpha) = K_I^2/(D\sigma_N^2)$ = dimensionless energy release rate function of LEFM reflecting the structure shape (K_I = mode I stress intensity factor, $E' = E$ for plane stress or $E/(1-\nu^2)$ for plane strain, E = Young's modulus, ν = Poisson ratio). Replacing the crack length a with the effective crack length $a = a_0 + c_f$ where c_f is a material constant characterizing the effective FPZ length, one gets $\mathcal{G} = (\sigma_N^2/E')Dg(\alpha_0 + c_f/D)$ where $\alpha_0 = a_0/D$ and a_0 = length of notch or open stress-free crack. Writing the first two terms of the Taylor series expansion, and setting $g_0 = g(\alpha_0)$ and $g_0' = \mathrm{d}g(\alpha_0)/\mathrm{d}\alpha$, one has $\mathcal{G} = (\sigma_N^2/E')D(g_0 + g_0'(c_f/D))$, which gives

$$\mathcal{G} = \mathcal{G}_s + \mathcal{G}_b \tag{57}$$

$$\text{where} \quad \mathcal{G}_s = (\sigma_N^2/E')Dg_0, \quad \mathcal{G}_b = (\sigma_N^2/E')c_f g_0' \tag{58}$$

Here $g_0 = g(\alpha_0), g_0' = [\mathrm{d}g(\alpha)/\mathrm{d}\alpha]_{\alpha_0}$. Noting that $\mathcal{G} = G_f$ = material fracture energy, we may solve for σ_N and, after rearrangements, obtain the Type 2 classical size effect law (Bažant, 1984b; Bažant et al., 1987; Bažant and Kazemi, 1991) for quasibrittle structures of geometrically similar shapes and cracks (or notches):

$$\sigma_N = \sqrt{\frac{E'G_f}{g_0'c_f + g_0 D}} = \frac{\sigma_0}{\sqrt{1 + D/D_0}} \tag{59}$$

Here $\sigma_0 = (E'G_f/c_f g_0')^{1/2}$ and $D_0 = (g_0'/g_0)c_f$ (transitional size). This law is now embodied in the concrete design code, ACI Standard 318/2019, for the scaling of brittle failures of concrete structures. The material characteristic length, c_f, of concrete has been shown to be about $0.4l_0$ for $\sigma_{xx} \approx 0$ (here $l_0 = E'G_f/\sigma_y^2$ = Irwin's characteristic length (Cusatis and Schauffert, 2011; Bažant and Yu, 2011)).

To fit test data, Eq. (59) is rearranged as a linear regression plot:

$$Y = AX + C \quad \text{where} \quad X = D,\ Y = 1/\sigma_N^2,\ A = 1/(\sigma_0^2 D_0),\ C = 1/\sigma_0^2 \tag{60}$$

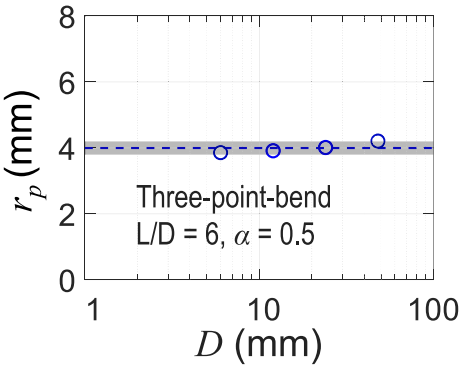

Fig. A.1. The dependence of the effective YZ's size r_p on the structure size D in specimens with three-point-bend configuration (Nguyen et al., 2021).

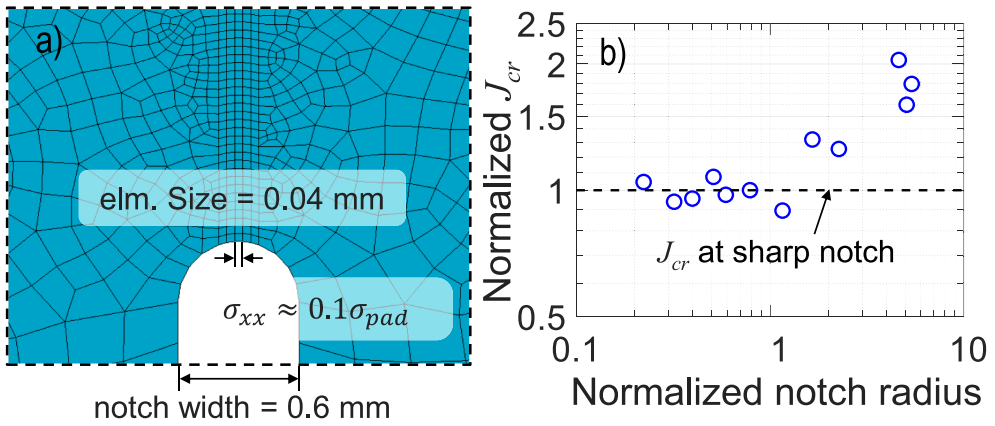

Fig. A.2. (a) The finite element mesh in front of the blunt notch tip. (b) The dependence of Alumina measured fracture energy on the notch radii normalized by the grain size, reproduced from Nishida et al. (1994), which serves as a qualitative reference point for the aluminum alloy used in this study.

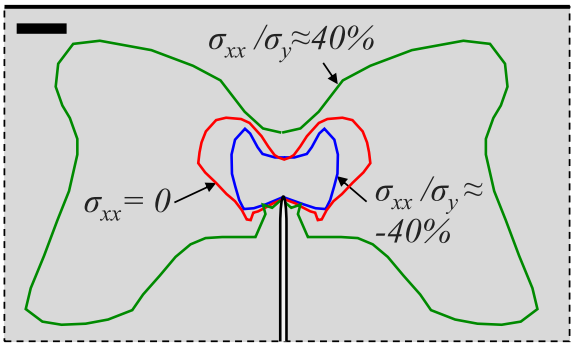

Fig. A.3. The evolution of the YZ with positive and negative σ_{xx} in the gap test configuration (the scale bar represents 5 mm).

Data regression yields A and C, and then one can evaluate G_f and c_f from the last equation. This method of measuring material fracture characteristics has become the international standard recommendation of RILEM (TC89-FMT, 1990) (also endorsed by the ACI-446 Committee), and is in wide use. Eqs. (59) can be used even when structures of different sizes D are not geometrically similar, but a different $g(\alpha)$ must then be used for various specimens.

Note that the effective size c_f cannot distinguish the length and width of the FPZ because both have a similar effect on the energy release rate. The fact that changing the FPZ width has a similar effect as changing c_f which is demonstrated by analysis based on configurational forces (Bažant, 1990). One should also realize that the FPZ width should be more than d_c and less than about $10d_c$ where d_c = inhomogeneity size (here the crystal size, about 0.5 μm); $3d_c$ is a reasonable guess (Bažant et al., 1984).

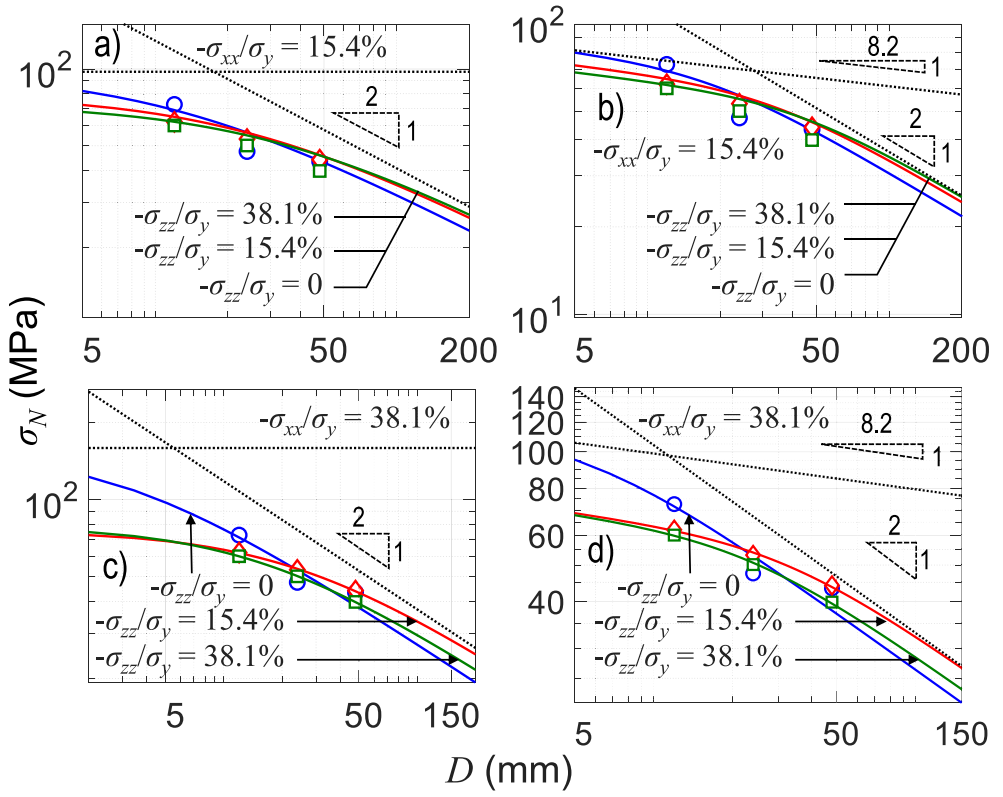

Fig. A.4. The fitting of the scaling law in Eq. (23) (a,c) and Eq. (34) (b,d) against numerical predictions based on the constitutive law in Bai and Wierzbicki (2010) (both extrinsic σ_{xx} and σ_{zz}).

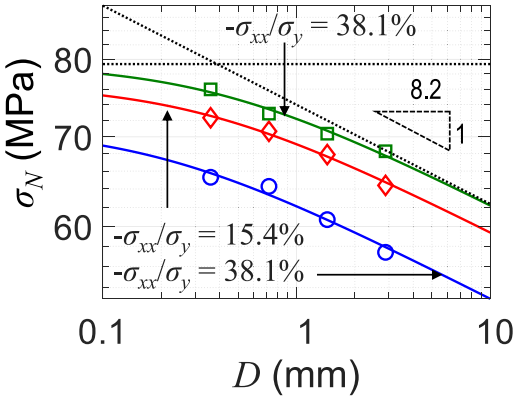

Fig. A.5. The fitting of the scaling law in Eq. (40) against numerical predictions based on the constitutive law in Bai and Wierzbicki (2010) (extrinsic σ_{xx} only).

Appendix B. Comments on 1970s Westinghouse's experiments on geometrically scaled specimens

The asymptotic matching as $D \to \infty$ in this study and Nguyen et al. (2021) receives additional support from large scaling experiment on steel carried out at Westinghouse company in the mid 1970s (see Fig. A.6). These experiments were intended to identify the size at which the LEFM is valid, and thus the fracture energy G_f of steel becomes equal to the critical value J_{cr} of the J-integral.

The tests showed that the J_{cr} was equal to G_f for the largest specimen size shown in figure. For smaller specimens this was not the case (partly because, as already mentioned here and found long ago, the compact-tension specimens experience appreciable non-zero "intrinsic" T-stresses).

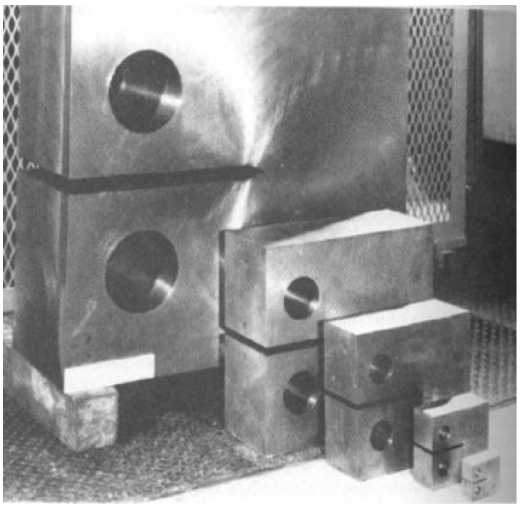

Fig. A.6. Compact-tension tests with geometrically scaled specimens at Westinghouse (private communication through professor Jimmy Hsia (Editor, JMPS), NTU, Singapore.

Unfortunately, the data from these classical tests of various size were, apparently, not published—perhaps because, in the 1970s, the research community was not interested in the scaling problems of solid mechanics.

Appendix C. Calculation of dimensionless angular functions and work expressions in classical HRR theory

The expressions for angular functions in Eqs. (10)–(12) were not presented in the preceding study (Nguyen et al., 2021). However, they are needed to predict the mechanical response and size effect of the structural-scale strength when experimental data for calibration are unavailable or scant. Calculating the partial derivatives in the linearized strain expression $e_{ij} = \frac{1}{2}(u_{i,j} + u_{j,i})$, one finds that the dimensionless angular function in Eq. (11) is:

$$\varphi_{ij}(\theta) = \frac{1}{2}\left\{ \frac{F_i(\theta)\xi_j(\theta) + F_j(\theta)\xi_i(\theta)}{n+1} + F_i'(\theta)\xi_j^{\perp}(\theta) + F_j'(\theta)\xi_i^{\perp}(\theta) \right\} \tag{61}$$

where $\boldsymbol{\xi}(\theta)$ and $\boldsymbol{\xi}^{\perp}(\theta)$ are the unit position vector and its orthogonal counterpart. Functions F_i could, in theory, be also calculated from functions φ_{ij}. However, it would involve solving a stress function that satisfies Eqs. (10)–(12) and boundary conditions numerically.

Because the Ramberg–Osgood constitutive law, Eq. (3), does not allow expressing s_{ij} in terms of e_{ij} explicitly, the calculation of strain energy density, $\overline{W} = \int s_{ij}\mathrm{d}e_{ij}$, is facilitated if we first calculate the density of complementary strain energy (or Gibbs free energy), which is defined as $W^* = \int e_{ij}\mathrm{d}s_{ij}$. Since it is path-independent, we get a general result even if we conveniently integrate along a proportional loading path, $s_{ij} = S_{ij}\mu$ where S_{ij} are constants, the loading parameter, μ, runs from 0 to 1, and $S_{ij} = [s_{ij}]_{\mu=1}$. This way, $\overline{W}$ becomes a integral over μ only. Noting Eqs. (11) and (12) and integrating, we get

$$W^* = \frac{\alpha_p \epsilon_y}{(n+1)\sigma_y^n}\left(\frac{3}{2}\, s_{ij}s_{ij}\right)^{\frac{n+1}{2}} \tag{62}$$

The density $\overline{W}$ of strain energy (or Helmholtz free energy) is a function of e_{ij}. However, since it is impossible to invert Eq. (3) in a closed form, we must express $\overline{W}$ in terms of s_{ij}. We can do so exploiting Legendre transformation $\overline{W} = s_{ij}e_{ij} - W^*$, which is derived by integrating $\int e_{ij}\mathrm{d}s_{ij}$ by parts. This gives

$$\overline{W} = \frac{n\alpha_p \epsilon_y}{(n+1)\sigma_y^n}\left(\frac{3}{2}\, s_{ij}s_{ij}\right)^{\frac{n+1}{2}} \tag{63}$$

Here s_{ij} must be regarded as functions of e_{ij}, given implicitly by Eq. (3). To obtain the J-integral, we must also evaluate

$$\nu_j s_{ij} u_{i,1} = \nu_j \alpha_p \epsilon_y \sigma_y \left(\frac{r}{r_p}\right)^{-1} \psi_{ij}(\theta)\chi_i(\theta) \tag{64}$$

where $$\chi_i(\theta) = \frac{F_i(\theta)}{n+1}\,\xi_1(\theta) + F_i'(\theta)\xi_1^{\perp}(\theta) \tag{65}$$

The J-integral may now be calculated at $r = r_p$:

$$J = \alpha_p \epsilon_y \sigma_y r_p \kappa \tag{66}$$

$$\text{where } \kappa = \int_{-\pi}^{\pi} \left[\nu_1 \frac{n}{n+1} \left(\frac{3}{2} \psi_{ij}(\theta)\psi_{ij}(\theta) \right)^{\frac{n+1}{2}} - \nu_j \psi_{ij}(\theta)\chi_i(\theta) \right] \mathrm{d}\theta \tag{67}$$

Note that, instead of the radius r_p' of the T-modified energy matching zone, one must use the effective YZ radius r_p. Evaluation of $\iint$[Eq. (15)] $r\,\mathrm{d}\theta\,\mathrm{d}r$ shows that the total strain energy in the circle of radius r_p per unit width in the transverse direction, is expressed as

$$W = \frac{n}{n+1} \alpha_p \sigma_y \epsilon_y r_p^2 \int_{-\pi}^{\pi} \varphi_{ij}(\theta)\psi_{ij}(\theta)\mathrm{d}\theta \tag{68}$$

Appendix D. Effect of notch width, or crack bluntness, on fracture parameters

The notch bluntness is known to increase the specimen ductility and affect the fracture parameters (Nishida et al., 1994), as the material response shifts toward material strength domination (see Fig. A.2b). For the fracture and size effect tests of quasibrittle materials such as concrete, it is known that the fracture parameters measured will not be affected if the width of the notch front is less than about 1/3 of the maximum size of the material inhomogeneity (or mineral aggregate).

This condition is easy to satisfy for concrete. However, for polycrystalline metals, in which the crystals size is of the order of up to a few tens of micrometers, achieving sufficient notch sharpness is a challenge.

Appendix E. A brief summary of Bai–Wierzbicki damage constitutive model for metal

To characterize the behavior of aluminum alloy for different structural sizes and different crack-parallel stress levels, one needs a damage constitutive law for the FPZ of aluminum under complex triaxial stress states. For that, the best existing model seems to be the model of Bai and Wierzbicki (2010). Its key points follow.

In this model, the Mohr–Coulomb (M–C) fracture criterion is used to describe the onset of ductile fracture in aluminum as an isotropic material initially free of microcracks. This criterion has been extensively used in rock and soil mechanics as it correctly accounts for the effects of hydrostatic pressure as well as the Lode angle. It turns out that these two parameters, which are critical for characterizing the fracture of geomaterials, are also useful for the fracture of ductile metals (Bai and Wierzbicki, 2008; Xue, 2007; Barsoum, 2006; Wilkins et al., 1980). The local Cartesian form of the M–C criterion is transformed to the spherical coordinate system, where the axes are the equivalent strain to fracture strain $\bar{\epsilon}_f$, the stress triaxiality η and the normalized Lode angle parameter $\bar{\theta}$. For the proportional loading, the fracture surface is shown to be an asymmetric function of $\bar{\theta}$. The M–C fracture criterion is found to predict almost exactly the exponential decay of material ductility with stress triaxiality, which is in accordance with the theoretical analysis of Rice and Tracey (1969) and with the empirical equations of Hancock and Mackenzie (1976) and Johnson and Cook (1985). The M–C criterion also predicts a form of Lode angle dependence that is close to parabolic. The results for the tested aluminum alloy were used to calibrate and validate the proposed M–C fracture model (Bai and Wierzbicki, 2010).

Another advantage of the M–C fracture model is that it predicts uniquely the orientation of the fracture surface. The direction cosines of the unit normal vector of the fracture surface are functions of the "friction" coefficient in the M–C criterion. In the M-C criterion, the three relevant parameters are three invariants of the stress tensor $\boldsymbol{\sigma}$ defined by (Bai and Wierzbicki, 2008):

$$p = -\sigma_m = -\frac{1}{3}\,\mathrm{tr}([\sigma]) = -\frac{1}{3}\left(\sigma_1 + \sigma_2 + \sigma_3\right) \tag{69}$$

$$q = \bar{\sigma} = \sqrt{\frac{3}{2}\mathbf{S} : \mathbf{S}} = \sqrt{\frac{1}{2}\left[\left(\sigma_1 - \sigma_2\right)^2 + \left(\sigma_2 - \sigma_3\right)^2 + \left(\sigma_3 - \sigma_1\right)^2\right]}$$

$$r = \left(\frac{9}{2}\mathbf{S}\cdot\mathbf{S} : \mathbf{S}\right)^{1/3} = \left[\frac{27}{2}\det(\mathbf{S})\right]^{1/3} = \left[\frac{27}{2}\left(\sigma_1 - \sigma_m\right)\left(\sigma_2 - \sigma_m\right)\left(\sigma_3 - \sigma_m\right)\right]^{1/3} \tag{70}$$

where $\mathbf{S}$ is the deviatoric tensor. The dimensionless hydrostatic pressure η and the normalized Lode angle are defined by:

$$\eta = \frac{-p}{q} = \frac{\sigma_m}{\bar{\sigma}} \tag{71}$$

$$\bar{\theta} = 1 - \frac{6\theta}{\pi} = 1 - \frac{2}{\pi}\arccos\left(\frac{r}{q}\right)^3 \tag{72}$$

The extended plasticity is described by:

$$2\bar{\sigma}_y^{2k} = \left(\sigma_1 - \sigma_2\right)^{2k} + \left(\sigma_2 - \sigma_3\right)^{2k} + \left(\sigma_3 - \sigma_1\right)^{2k} \tag{73}$$

$$\bar{\sigma} = A\bar{\varepsilon}^n \left[1 - c_\eta\left(\eta - \eta_0\right)\right]\left[c_\theta^s + \left(c_\theta^{ax} - c_\theta^s\right)\gamma\right] \tag{74}$$

$$c_\theta^{ax} = \begin{cases} 1 & \text{for } \bar{\theta} \geq 0 \\ c_\theta^c & \text{for } \bar{\theta} < 0 \end{cases} \tag{75}$$

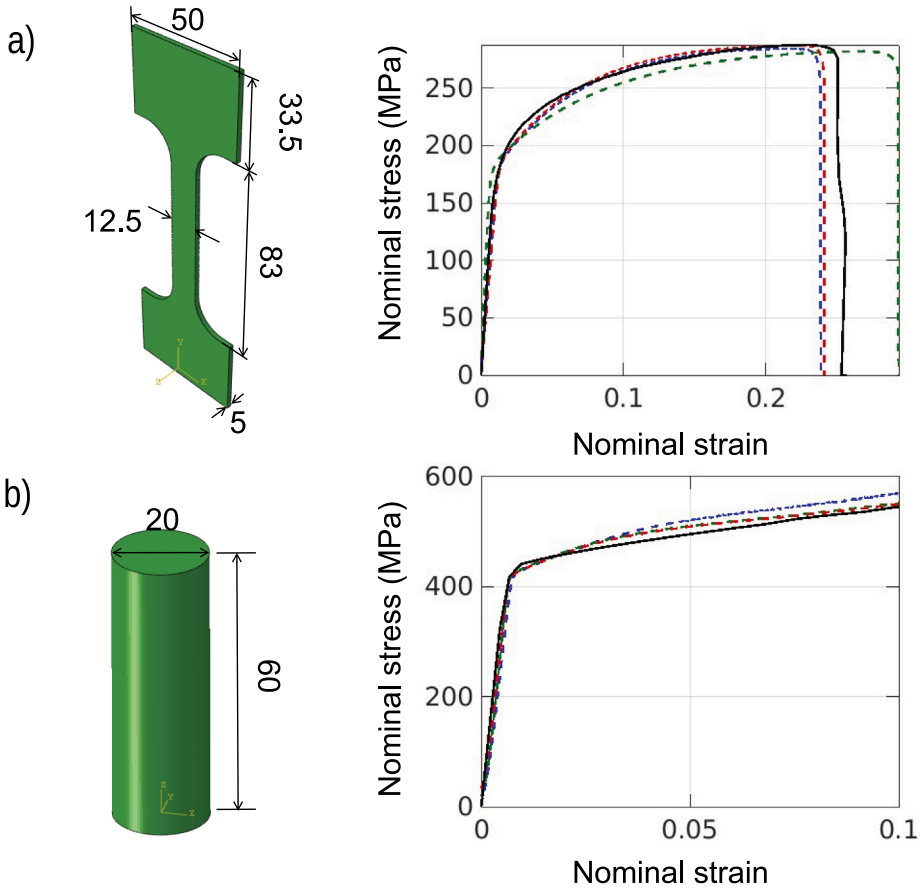

Fig. A.7. Characterization experiments of Al 6061-T651 and the fitting of Bai–Wierzbicki's model for specimens subjected to (a) uniaxial tension and (b) compression.

Table 1
Parameters for Bai–Wierzbicki damage constitutive model.

E	ν	m	A	ϵ_y	N	D_c	c_1	c_2
72 000.	0.334	6.	450.	0.0068	0.097	1.001	0.6	510.
$\bar{c}_\theta^s$	c_g	η_{cutoff}	c_η	η_0	c_θ^s	c_θ^c		
0.922	0.001	1.	0.05	0.3333	1.	1.		

Finally, the constitutive relation can be summarized as:

$$\bar{\varepsilon}_f = \left\{ \frac{A}{c_2}\left[1 - c_\eta\left(\eta - \eta_o\right)\right]\left[c_\theta^s + \frac{\sqrt{3}}{2-\sqrt{3}}\left(c_\theta^{ax} - c_\theta^s\right)\left(\sec\left(\frac{\bar{\theta}\pi}{6}\right) - 1\right)\right] \left[\sqrt{\frac{1+c_1^2}{3}}\cos\left(\frac{\bar{\theta}\pi}{6}\right) + c_1\left(\eta + \frac{1}{3}\sin\left(\frac{\bar{\theta}\pi}{6}\right)\right)\right]\right\}^{-\frac{1}{n}}$$

Appendix F. Results of the characterization tests of aluminum alloy 6060-T651

The parameters necessary to define the functions in Appendix E can be found in Bai and Wierzbicki (2010) and their values are presented in Table 1.

The parameters in Table 1 were optimized to capture the characterization results in Figs. A.7 and the size effect results in Nguyen et al. (2021) and the gap test with $\sigma_{xx} = 0$ in Fig. 9.

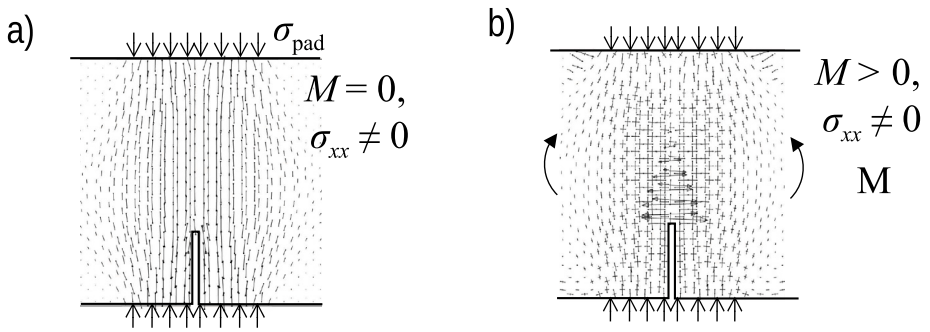

Fig. A.8. The distribution of principal stresses when (a) $M = 0, \sigma_{pad} \neq 0$ and (b) $M > 0, \sigma_{pad} \neq 0$.

Appendix G. Other details of the gap tests for aluminum alloy

The grain size, as well as the material microstructure of a specific metallic material, depends on the chemical element of metal, the alloy stoichiometry, and metal purity. In addition, depending on the manufacturing and processing methods, the FPZ size of the same alloy type may vary widely, as already mentioned in the introduction (Shankar et al., 2005; Zhang et al., 2018). In this study, the grain size is taken as 40 μm, which gives optimum fits of the characterization tests of alloy 6061-T651, including the uniaxial compression, direct tension, and size effect tests σ_{xx} (see Nguyen et al. (2021, Fig. 5), Fig. 3 and Appendix D for the fitting details). While grain size analyses using the optical and electron microscope can be found elsewhere (Zhang et al., 2018; Rathinasuriyan et al., 2019), relating these analyses to the present material fracture properties would be a major task beyond the scope of the present study.

The size-effect experiments at any structure size were J-controlled, as evidenced by the match of the J-values measured at the peak load for all specimens sizes (Nguyen et al., 2021) and also those computed using the size effect law. This has been shown in the previous studies (Nguyen et al., 2021; Bažant et al., 1987), which are extended here. In addition, Fig. A.3 showed that the yielding zone dominated the crack tip region in most cases, which documents the J-controlled nature of the crack growth at least up to the peak load. For these reasons, and because of the fact that the size effect tests serve to be an alternative to the conventional J-measurement techniques (ASTM-E1820, 2020), the J vs. Δa measurements appeared to be redundant.

Although the stress–strain fields at the crack front were not mapped experimentally, the depiction of these fields in the numerical simulations shown in Fig. A.8 should suffice to show that the crack-parallel stress distribution was nearly uniform within the HRR field. Extracting accurate stress–strain fields from the experiments in the pre-peak regime calls for techniques that can provide high-resolution displacement fields (down to sub-micrometer per pixel) such as electronic speckle pattern interferometry (Gåsvik, 2003) or high resolution digital image correlation (Carroll et al., 2013), which alone would require a major separate experimental effort.

References

Anderson, T.L., 1991. Fracture Mechanics: Fundamentals and Applications. CRC Press, Boca Raton, FL.
ASTM-E1820, 2020. Standard Test Method for Measurement of Fracture Toughness. Standard, American Society for Testing and Materials, West Conshohocken, PA.
Bai, Y., Wierzbicki, T., 2008. A new model of metal plasticity and fracture with pressure and Lode dependence. Int. J. Plast. 24 (6), 1071–1096.
Bai, Y., Wierzbicki, T., 2010. Application of extended Mohr–Coulomb criterion to ductile fracture. Int. J. Fract. 161 (1), 1–20.
Bao, Y., Wierzbicki, T., 2004. On fracture locus in the equivalent strain and stress triaxiality space. Int. J. Mech. Sci. 46 (1), 81–98.
Barenblatt, G., 1979. Similarity, Self-Similarity, and Intermediate Asymptotics. Consultants Bureau, New York.
Barsoum, I., 2006. Ductile Failure and Rupture Mechanisms in Combined Tension and Shear (Ph.D. thesis). Hållfasthetslära.
Bažant, Z.P., 1984a. Imbricate continuum and its variational derivation. J. Eng. Mech. 110 (12), 1693–1712.
Bažant, Z.P., 1984b. Size effect in blunt fracture: concrete, rock, metal. J. Eng. Mech. 110 (4), 518–535.
Bažant, Z.P., 1990. Justification and improvement of Kienzler and Herrmann's estimate of stress intensity factors of cracked beam. Engineering Fracture Mechanics 36 (3), 523–525.
Bažant, Z.P., 1993. Scaling laws in mechanics of failure. J. Eng. Mech. 119 (9), 1828–1844.
Bažant, Z.P., 1996. Size effect aspects of measurement of fracture characteristics of quasibrittle material. Adv. Cem. Based Mater. 4 (3–4), 128–137.
Bažant, Z.P., 2005. Scaling of Structural Strength, second ed. Elsevier Science.
Bažant, Z.P., Belytschko, T.B., Chang, T.-P., 1984. Continuum theory for strain-softening. J. Eng. Mech. 110 (12), 1666–1692.
Bažant, Z.P., Cedolin, L., 1979. Blunt crack band propagation in finite element analysis. J. Eng. Mech. Div. 105 (2), 297–315.
Bažant, Z.P., Chen, E.-P., 1997. Scaling of structural failure. Appl. Mech. Rev. ASME 50 (10), 593–627.
Bažant, Z.P., Dönmez, A.A., Nguyen, H.T., 2022. Précis of gap test results requiring reappraisal of line crack and phase-field models of fracture mechanics. Eng. Struct. 250, 113285.
Bažant, Z.P., Estenssoro, L.F., 1979. Surface singularity and crack propagation. Int. J. Solids Struct. 15 (5), 405–426.
Bažant, Z.P., Kazemi, M.T., 1991. Size effect on diagonal shear failure of beams without stirrups. ACI Struct. J. 88 (3), 268–276.
Bažant, Z.P., Le, J.-L., Salviato, M., 2021. Quasibrittle Fracture Mechanics and Size Effect: A First Course. Oxford University Press.
Bažant, Z.P., Lee, S.-G., Pfeiffer, P.A., 1987. Size effect tests and fracture characteristics of aluminum. Eng. Fract. Mech. 26 (1), 45–57.
Bažant, Z.P., Oh, B.H., 1983. Crack band theory for fracture of concrete. Matér. Constr. 16 (3), 155–177.

Bažant, Z.P., Planas, J., 1998. Fracture and Size Effect in Concrete and Other Quasibrittle Materials. In: New Directions in Civil Engineering, CRC Press, Boca Raton and New York.
Bažant, Z.P., Yu, Q., 2011. Size-effect testing of cohesive fracture parameters and non-uniqueness of work-of-fracture method. ASCE J. Eng. Mech. 137 (8), 580–588.
Benzerga, A., Surovik, D., Keralavarma, S., 2012. On the path-dependence of the fracture locus in ductile materials–analysis. Int. J. Plast. 37, 157–170.
Betegón, C., Hancock, J.W., 1991. Two-parameter characterization of elastic-plastic crack-tip fields. J. Appl. Mech. 58 (1), 104–110.
Brockmann, J., Salviato, M., 2022. The gap test–effects of crack parallel compression on fracture in carbon fiber composites. Composites A 107252.
Carroll, J.D., Abuzaid, W., Lambros, J., Sehitoglu, H., 2013. High resolution digital image correlation measurements of strain accumulation in fatigue crack growth. Int. J. Fatigue 57, 140–150.
Cusatis, G., Schauffert, E.A., 2011. Cohesive crack analysis of size effect. Eng. Fract. Mech. 76 (14), 2163–2173.
Dönmez, A.A., 2021a. Size effect on inclined cracking in unidirectional composites. J. Appl. Comput. Mech. 7 (4), 2149–2158.
Dönmez, A.A., 2021b. Size effect on the shear capacity of headed studs. Adv. Struct. Eng. 24 (4), 815–826.
Gao, X., Shih, C., Tvergaard, V., Needleman, A., 1996. Constraint effects on the ductile-brittle transition in small scale yielding. J. Mech. Phys. Solids 44 (8), 1255–1282.
Gåsvik, K.J., 2003. Optical Metrology. John Wiley & Sons.
Gupta, M., Alderliesten, R., Benedictus, R., 2015. A review of T-stress and its effects in fracture mechanics. Eng. Fract. Mech. 134, 218–241.
Gurson, A.L., 1977. Continuum theory of ductile rupture by void nucleation and growth: Part I—Yield criteria and flow rules for porous ductile media.
Hall, E.O., 1951. The deformation and ageing of mild steel: III discussion of results. Proc. Phys. Soc. Sect. B 64 (9), 747.
Hancock, J., Mackenzie, A., 1976. On the mechanisms of ductile failure in high-strength steels subjected to multi-axial stress-states. J. Mech. Phys. Solids 24 (2–3), 147–160.
Hancock, J.W., Reuter, W.G., Parks, D.M., 1993. Constraint and toughness parameterized by T. In: ASTM Special Technical Publication, Vol. 1171. American Technical Publishers Ltd, p. 21.
Hutchinson, J.W., 1968a. Plastic stress and strain fields at a crack tip. J. Mech. Phys. Solids 16 (5), 337–342.
Hutchinson, J.W., 1968b. Singular behaviour at the end of a tensile crack in a hardening material. J. Mech. Phys. Solids 16 (1), 13–31.
Hutchinson, J.W., Paris, P.C., 1979. Stability analysis of J-controlled crack growth. In: Elastic-Plastic Fracture. ASTM International.
Johnson, G.R., Cook, W.H., 1985. Fracture characteristics of three metals subjected to various strains, strain rates, temperatures and pressures. Eng. Fract. Mech. 21 (1), 31–48.
Joyce, J.A., Link, R.E., 1995. Effects of constraint on upper shelf fracture toughness. In: ASTM Special Technical Publication, Vol. 1256. American Technical Publishers Ltd, pp. 142–177.
Kanninen, M.F., Popelar, C.H., 1985. Advanced Fracture Mechanics. In: Oxford Engineering Science Series, Oxford University Press, New York.
Kim, H.-G., Chew, H.B., Kim, K.-S., 2012. Inverse extraction of cohesive zone laws by field projection method using numerical auxiliary fields. Internat. J. Numer. Methods Engrg. 91 (5), 516–530.
Kirk, M.T., Dodds, Jr., R.H., 1992. Approximate Techniques for Predicting Size Effects on the Cleavage Fracture Toughness (Jc). Tech. Rep., University of Illinois Engineering Experiment Station. College of ....
Krafft, J., Sullivan, A., Boyle, R., 1961. Effect of dimensions on fast fracture instability of notched sheets. In: Proceedings of the Crack Propagation Symposium, Vol. 1. pp. 8–26, sn.
Larsson, S.-G., Carlsson, A., 1973. Influence of non-singular stress terms and specimen geometry on small-scale yielding at crack tips in elastic-plastic materials. J. Mech. Phys. Solids 21 (4), 263–277.
Levy, N., Marcal, P., Ostergren, W.J., Rice, J.R., 1971. Small scale yielding near a crack in plane strain: a finite element analysis. Int. J. Fract. Mech. 7 (2), 143–156.
Li, F.Z., Shih, C.F., Needleman, A., 1985. A comparison of methods for calculating energy release rates. Eng. Fract. Mech. 21 (2), 405–421.
Liu, Z., Wang, X., Tang, J., Deng, C., Zhao, H., Chen, X., 2019. The effects of in-plane and out-of-plane constraints on JR curves for X80 steel: A study using clamped SENT specimens. Eng. Fract. Mech. 206, 342–358.
Lu, K., Meshii, T., 2014. Three-dimensional T-stresses for three-point-bend specimens with large thickness variation. Eng. Fract. Mech. 116, 197–203.
Lv, J., Yu, L., Du, W., Li, Q., 2018. Theoretical approach of characterizing the crack-tip constraint effects associated with material's fracture toughness. Arch. Appl. Mech. 88 (9), 1637–1656.
Matvienko, Y.G., 2014. The effect of the non-singular T-stress components on crack tip plastic zone under mode I loading. Procedia Mater. Sci. 3, 141–146.
Matvienko, Y.G., 2015. The effect of out-of-plane constraint in terms of the T-stress in connection with specimen thickness. Theor. Appl. Fract. Mech. 80, 49–56.
Miao, X.-T., Zhou, C.-Y., He, X.-H., 2017. In-plane and out-of-plane constraint for single edge notched bending specimen and cruciform specimen under uniaxial and biaxial loading. Fatigue Fract. Eng. Mater. Struct. 40 (12), 1945–1959.
Nakamura, T., Parks, D.M., 1992. Determination of elastic T-stress along three-dimensional crack fronts using an interaction integral. Int. J. Solids Struct. 29 (13), 1597–1611.
Narasimhan, R., Rosakis, A.J., 1990. Three-dimensional effects near a crack tip in a ductile three-point bend specimen: Part I—A numerical investigation. J. Appl. Mech. 57 (3), 607–617.
Nguyen, H.T., Dönmez, A.A., Bažant, Z.P., 2021. Structural strength scaling law for fracture of plastic-hardening metals and testing of fracture properties. Extreme Mech. Lett. 43, 101141.
Nguyen, H., Pathirage, M., Cusatis, G., Bažant, Z.P., 2020a. Gap test of crack-parallel stress effect on quasibrittle fracture and its consequences. J. Appl. Mech. 87 (7).
Nguyen, H., Pathirage, M., Rezaei, M., Issa, M., Cusatis, G., Bažant, Z.P., 2020b. New perspective of fracture mechanics inspired by gap test with crack-parallel compression. Proc. Natl. Acad. Sci. 117 (25), 14015–14020.
Nikishkov, G., 1998. J-a fracture concept based on the three-term elastic-plastic asymptotic expansion of the near-crack tip stress field. Fract.: Top. Encyclopedia Curr. Knowl. 557–574.
Nishida, T., Hanaki, Y., Pezzotti, G., 1994. Effect of notch-root radius on the fracture toughness of a fine-grained alumina. J. Am. Ceram. Soc. 77 (2), 606–608.
O'Dowd, N., Shih, C.F., 1991. Family of crack-tip fields characterized by a triaxiality parameter—I. Structure of fields. J. Mech. Phys. Solids 39 (8), 989–1015.
O'Dowd, N.P., Shih, C.F., 1992. Family of crack-tip fields characterized by a triaxiality parameter—II. Fracture applications. J. Mech. Phys. Solids 40 (5), 939–963.
Papasidero, J., Doquet, V., Mohr, D., 2015. Ductile fracture of aluminum 2024-t351 under proportional and non-proportional multi-axial loading: Bao–Wierzbicki results revisited. Int. J. Solids Struct. 69, 459–474.
Pineau, A., Benzerga, A.A., Pardoen, T., 2016a. Failure of metals I: Brittle and ductile fracture. Acta Mater. 107, 424–483.
Pineau, A., Benzerga, A.A., Pardoen, T., 2016b. Failure of metals III: Fracture and fatigue of nanostructured metallic materials. Acta Mater. 107, 508–544.
Pineau, A., McDowell, D.L., Busso, E.P., Antolovich, S.D., 2016c. Failure of metals II: Fatigue. Acta Mater. 107, 484–507.
Ramberg, W., Osgood, W.R., 1943. Description of Stress-Strain Curves by Three Parameters. Technical Note 902, NACA, Washington, D.C..
Rathinasuriyan, C., Sankar, R., Shanbhag, A.G., SenthilKumar, V., 2019. Prediction of the average grain size in submerged friction stir welds of AA 6061-T6. Mater. Today: Proc. 16, 907–917.
Revil-Baudard, B., Cazacu, O., Chandola, N., 2018. Effect of the yield stresses in uniaxial tension and pure shear on the size of the plastic zone near a crack. Int. J. Plast. 102, 101–117.

Rice, J.R., 1968a. A path independent integral and the approximate analysis of strain concentration by notches and cracks. ASME J. Appl. Mech. 35 (2), 379–386.
Rice, J.R., 1968b. Mathematical analysis in the mechanics of fracture. Fract.: Adv. Treatise 2, 191–311.
Rice, J., Rosengren, G.F., 1968. Plane strain deformation near a crack tip in a power-law hardening material. J. Mech. Phys. Solids 16 (1), 1–12.
Rice, J.R., Tracey, D.M., 1969. On the ductile enlargement of voids in triaxial stress fields. J. Mech. Phys. Solids 17 (3), 201–217.
Shankar, M.R., Chandrasekar, S., Compton, W.D., King, A.H., 2005. Characteristics of aluminum 6061-T6 deformed to large plastic strains by machining. Mater. Sci. Eng. A 410, 364–368.
Shen, G., Tyson, W., Glover, A., Horsley, D., 2005. Constraint effects on linepipe toughness. PICon J. 1.
Sobotka, J., Dodds, Jr., R., 2011. T-stress effects on steady crack growth in a thin, ductile plate under small-scale yielding conditions: Three-dimensional modeling. Eng. Fract. Mech. 78 (6), 1182–1200.
TC89-FMT, R.R., 1990. Size-effect method for determining fracture energy and process zone size of concrete. Mater. Struct. 23 (6), 461–465.
Tschegg, E., Elser, M., Stanzl-Tschegg, S., 1995. Biaxial fracture tests on concrete—development and experience. Cem. Concr. Compos. 17 (1), 57–75.
Tvergaard, V., 1989. Material failure by void growth to coalescence. Adv. Appl. Mech. 27, 83–151.
Wilkins, M., Streit, R., Reaugh, J., 1980. Cumulative-Strain-Damage Model of Ductile Fracture: Simulation and Prediction of Engineering Fracture Tests. Tech. Rep., Lawrence Livermore National Lab., CA (USA).
Williams, M.L., 1952. Stress singularities resulting from various boundary conditions in angular corners of plates in extension. J. Appl. Mech. 19 (4), 526–528.
Xia, L., Wang, T., Shih, C., 1993. Higher-order analysis of crack tip fields in elastic power-law hardening materials. J. Mech. Phys. Solids 41 (4), 665–687.
Xin, G., Hangong, W., Xingwu, K., Liangzhou, J., 2010. Analytic solutions to crack tip plastic zone under various loading conditions. Eur. J. Mech. A Solids 29 (4), 738–745.
Xue, L., 2007. Ductile Fracture Modeling: Theory, Experimental Investigation and Numerical Verification (Ph.D. thesis). Massachusetts Institute of Technology.
Yeh, H.-Y., Ahmed, K., Yeh, H.-L., 2006. Change of damage zone size by T-stress. J. Reinf. Plast. Compos. 25 (6), 645–661.
Yuan, H., Brocks, W., 1998. Quantification of constraint effects in elastic-plastic crack front fields. J. Mech. Phys. Solids 46 (2), 219–241.
Zehnder, A.T., Rosakis, A.J., 1990. Three-dimensional effects near a crack tip in a ductile three-point bend specimen: Part II—An experimental investigation using interferometry and caustics. J. Appl. Mech. 57 (3), 618–626.
Zhang, Z., Wang, J., Zhang, Q., Zhang, S., Shi, Q., Qi, H., 2018. Research on grain refinement mechanism of 6061 aluminum alloy processed by combined SPD methods of ECAP and MAC. Materials 11 (7), 1246.
Zhu, X.-K., Leis, B.N., 2006. Bending modified J–Q theory and crack-tip constraint quantification. Int. J. Fract. 141 (1), 115–134.